



HAL
open science

Upscaling of Elastic Properties in Carbonates: A Modeling Approach Based on a Multiscale Geophysical Data Set

Cedric Bailly, J. Fortin, M. Adelinet, Y. Hamon

► **To cite this version:**

Cedric Bailly, J. Fortin, M. Adelinet, Y. Hamon. Upscaling of Elastic Properties in Carbonates: A Modeling Approach Based on a Multiscale Geophysical Data Set. *Journal of Geophysical Research: Solid Earth*, 2019, 124 (12), pp.13021-13038. 10.1029/2019JB018391 . hal-02516786

HAL Id: hal-02516786

<https://ifp.hal.science/hal-02516786>

Submitted on 25 Mar 2020

HAL is a multi-disciplinary open access archive for the deposit and dissemination of scientific research documents, whether they are published or not. The documents may come from teaching and research institutions in France or abroad, or from public or private research centers.

L'archive ouverte pluridisciplinaire **HAL**, est destinée au dépôt et à la diffusion de documents scientifiques de niveau recherche, publiés ou non, émanant des établissements d'enseignement et de recherche français ou étrangers, des laboratoires publics ou privés.

1
2
3
4
5
6
7
8
9
10
11
12
13
14
15
16

**Upscaling of elastic properties in carbonates:
a modeling approach based on a multi-scale geophysical dataset**

C. Bailly^{1,2}, J. Fortin², M. Adelinet¹ and Y. Hamon¹

¹ IFP Energies nouvelles, Direction Géosciences, 1 et 4 Avenue de Bois-Préau, 92852 Rueil-Malmaison Cedex, France

²Laboratoire de Géologie, Ecole normale supérieure/CNRS UMR8538, PSL Research University, Paris 75005, France

Corresponding author: Cédric Bailly (bailly@geologie.ens.fr)

Key Points:

- Acquisition of multi-scale P-wave velocities at seismic, sonic and ultrasonic frequencies from the field to the lab at a single study site
- P-wave velocity decrease from ultrasonic to seismic frequencies with an increasing representative elementary volume
- Crack/fracture porosity control on the P-wave velocity at sonic and seismic scales leads to loss of matrix porosity control

17 **Abstract**

18 Linking ultrasonic measurements made in the laboratory on samples, with sonic logs and seismic
19 subsurface data is a key challenge for the understanding of carbonate reservoirs. To deal with this problem,
20 we investigate the elastic properties of dry lacustrine carbonates. At one study site, we perform a seismic
21 refraction survey (100 Hz), as well as “sonic” (54 kHz) and ultrasonic (250 kHz) measurements directly on
22 outcrop and ultrasonic measurements on samples in the laboratory (500 kHz). By comparing the median of
23 each dataset, we show that the P-wave velocity decreases from laboratory to seismic scale. Nevertheless,
24 the median of the sonic measurements acquired on outcrop surfaces seem to fit with the seismic data,
25 meaning that sonic acquisition may be representative of seismic scale. To explain the variations with
26 upscaling, we relate the concept of Representative Elementary Volume (REV) with the wavelength of each
27 scale of study. Indeed, the wavelength varies from millimetric at ultrasonic scale to pluri-metric at seismic
28 scale. This change of scale allows us to conclude that the behavior of P-wave velocity is due to different
29 geological features (matrix porosity, cracks, fractures) related to the different wavelengths used. Based on
30 effective medium theories, we quantify the pore aspect ratio at sample scale and the crack/fracture density
31 at outcrop and seismic scales using a multi-scale REV concept. Results show that the matrix porosity that
32 controls the ultrasonic P-wave velocities is progressively lost with upscaling, implying that crack and
33 fracture porosity impacts sonic and seismic P-wave velocities, a result of paramount importance for seismic
34 interpretation based on deterministic approaches.

35

36 1. Introduction

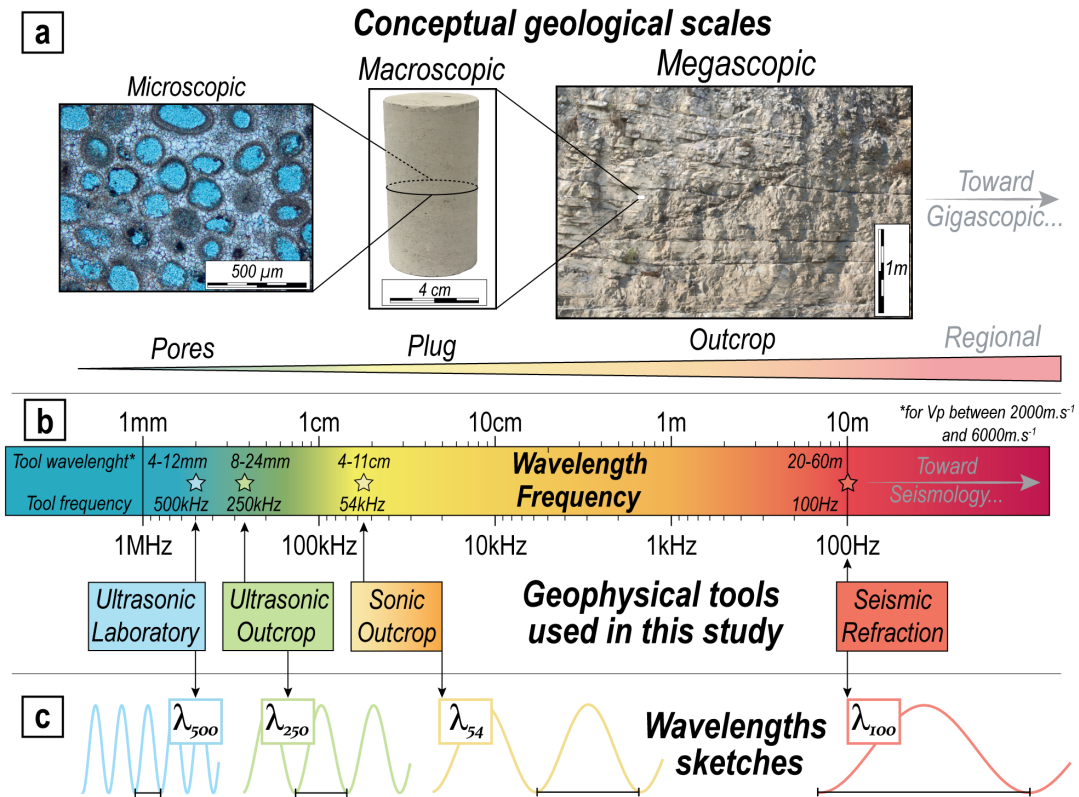
37

38 For isotropic rocks in dry conditions, upscaling of elastic properties can be done on the assumption
39 that the velocity acquired at ultrasonic (MHz), sonic (kHz) and seismic (Hz) frequencies are the same.
40 Indeed, if the investigated porous medium is homogeneous and dry, it is theoretically not dispersive, *i.e.*
41 the velocity does not depend on the frequency (Bourbié et al., 1987). This assumption is widely used in the
42 literature (*e.g.* Wang et al., 1991; Marion and Jizba, 1997; Baechle et al., 2005; Adam et al., 2006; Verwer
43 et al., 2008; Adelinet et al., 2011; Regnet et al., 2015 Borgomano et al., 2017) for inferring frequency
44 dispersion of elastic wave velocity in homogeneous porous and fluid saturated rocks.

45 This equality of dry elastic moduli at all frequencies is only valid if the Representative Elementary
46 Volume is uniform at each investigated scale (REV: volume of rock for which a physical property is
47 constant, *e.g.* Bear, 1972), in other words if a rock is homogeneous at all scales. As outlined by Corbett
48 (2009), this statement is far from true in geological medium which present “multiple length scales and
49 multiple scales of homogenization”. Indeed, following the conceptual geological scales of Haldorsen and
50 Lake (1984), several scales of geological heterogeneities exist (Figure 1a), including : i) the microscopic
51 scale (*i.e.* pore scale, μm to mm); ii) the macroscopic scale (*i.e.* the plug scale, cm); iii) the megascopic
52 scale (*i.e.* outcrop scale, m to dm) until iv) the gigascopic scale (*i.e.* regional scale, km).

53 These different geological scales imply different heterogeneities that may impact the upscaling of the
54 elastic properties of rocks. This point is of importance for the characterization of reservoirs based on a
55 deterministic approach, *i.e.* the use of velocity-porosity relationships based on laboratory and/or well data
56 (*e.g.* Wyllie et al., 1956; Raymer et al., 1980; Anselmetti and Eberli, 1993) for inferring petrophysical
57 properties (like porosity) from seismic data through impedance inversion (*e.g.* Marion and Jizba, 1997;
58 Cichostępski et al., 2019). Indeed, as outlined by Wollner and Dvorkin (2018), a rock-physics model built
59 from a given scale (*i.e.* centimetric in the laboratory) may not be applicable to another scale (*i.e.* pluri-metric
60 at seismic). According to Matonti et al. (2015), the direct comparison of P-wave velocities acquired on
61 carbonates at two different scales (plug *versus* outcrop) highlights a decrease of the P-wave velocity with

62 scale. These authors pointed out here a “scale effect” that they partly attribute to the presence of structural
 63 features (fractures). This finding joins the conclusions of previous authors, who suggest that the presence
 64 of cracks/fractures in crystalline rocks, due to upscaling, decrease of P-wave velocity (Stierman and
 65 Kovach, 1979; Moos and Zobach, 1983).



66 **Figure 1.** Comparison between upscaling in geology and geophysics. (a) Conceptual geological scales
 67 (from Haldorsen and Lake, 1984), highlighting the different scales of heterogeneities, including
 68 microscopic scale (pore size), macroscopic scale (plug size), megascopic (outcrop size) toward gigascopic
 69 scale (*i.e.* regional scale). (b) Frequencies and wavelengths for an elastic wave propagating at ultrasonic,
 70 sonic and seismic scales at a velocity of 1000 m.s⁻¹. The four different scales investigated in the present
 71 study are highlighted in different colored stars. They are associated with their frequencies and wavelengths
 72 for a P-wave velocity ranging between 2000 and 6000 m.s⁻¹. (c) Wavelength sketches of the four different
 73 scales studied on this work.

75
 76 Indeed, a P or S wave velocity measurement is representative of the elastic properties at a scale close
 77 to the wavelength. On one hand, seismic measurements (low frequency, f , and thus large wavelength - $\lambda=c/f$,
 78 where c is the velocity of the wave - in the order of several meters) will tend to erase small scale
 79 heterogeneities (Sheriff, 2002) (Figure 1b,c). On the other hand, ultrasonic measurements (high frequency,
 80 small wavelength) on samples are representative of the elastic properties at a scale of the order of the

81 millimeter (Figure 1b,c). Using a multi-scale geophysical dataset, it is thus possible to relate the elastic
82 properties acquired at different frequencies, and so defining effective elastic properties at different scales
83 of investigation. This purpose follows the previous works of Nordahl & Ringrose (2008) and Ringrose et
84 al. (2008) who argued that a multiscale geological medium has to be related to multiscale REVs. A
85 fundamental challenge here is to measure elastic properties of the same geological object across all scales
86 (Corbett, 2009). To do so, we study Miocene lacustrine carbonates from Samos Island (Greece).

87 We measure their dynamic elastic properties using several geophysical tools at different scales, from
88 field to laboratory (Figure 1): seismic refraction method (~ 100 Hz), sonic/ultrasonic measurements directly
89 on outcrop (54 kHz and 250 kHz), and ultrasonic measurements on plugs (500 kHz). These measurements
90 enable us to link and discuss the impact of different geological features (such as pores, cracks and fractures)
91 on the measured P-wave velocities from millimetric scale to decametric scales. Finally, based on asymptotic
92 approximations of Differential Elementary Medium scheme (DEM, David and Zimmerman, 2011a,b), we
93 compare the multi-scale elastic properties of the studied carbonates using a concept of multi-scale REVs
94 that take into account different scales of heterogeneities. In the following manuscript, the terms “cracks”
95 and “fractures” will refer to the occurrence and modeling of very low aspect ratio inclusions isotropically
96 distributed. The cracks correspond to small-scale inclusions (mm to cm scale) while the fractures are
97 attributed to large-scale inclusions (dm to m scale).

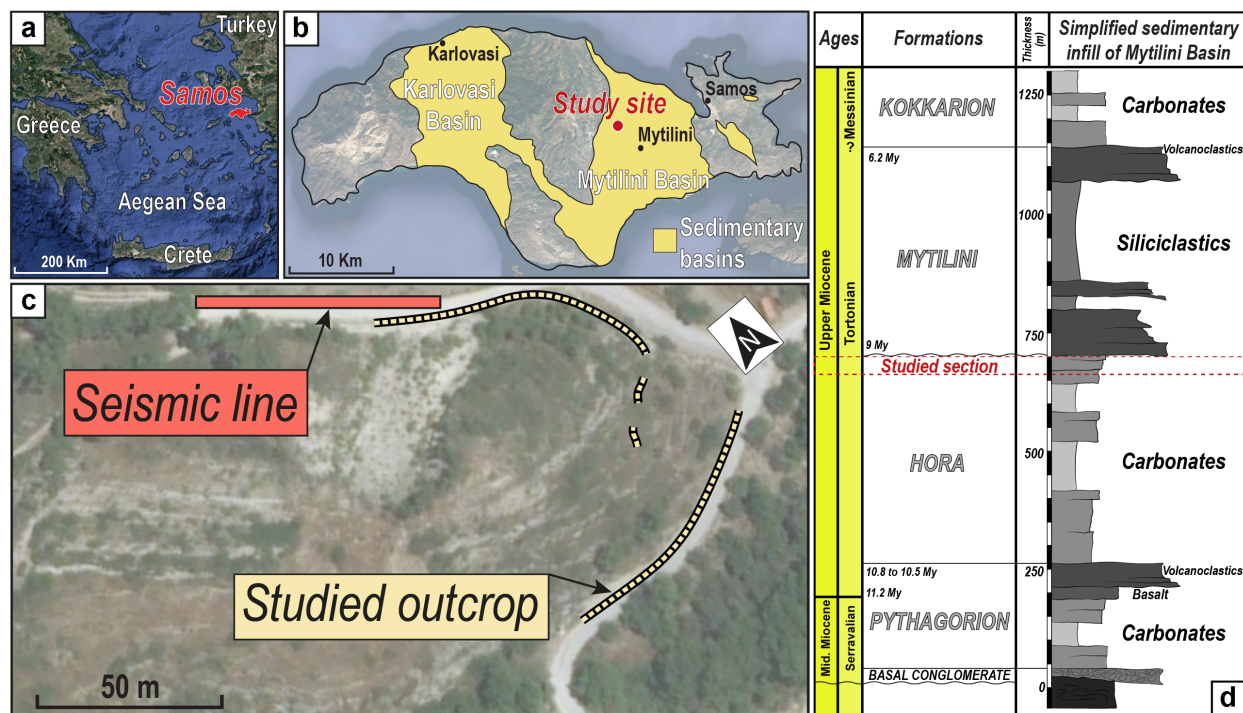
98

99 **2. Study framework**

100 Our study is focused on lacustrine carbonates of Samos, a Greek island located on the eastern part of the
101 Aegean Sea, near Turkey (Figure 2a). This island presents two sedimentary basins in which lacustrine
102 sedimentation occurred during the Upper Miocene (Weidman et al., 1984). Figure 2b points out the study
103 site on which we perform a seismic survey together with an outcrop description (Figure 2c). This study site
104 is localized on the Mytilini Basin, infilled with a huge diversity of rocks (such as volcanoclastic, siliciclastic
105 and carbonate rocks, Figure 2d). Our study focuses on the topmost part of the Hora Formation composed

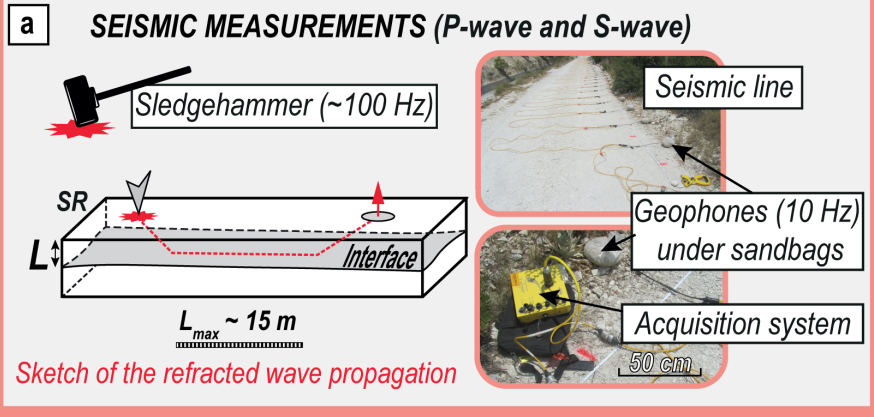
106 of lacustrine and palustrine carbonates (Figure 2d). These carbonates are deposited right before a major
 107 exposure, expressed as an erosional surface (Hora-Mytilini transition) according to Weidman et al. (1984)
 108 and Stamatakis et al. (1989). This emergence may result from a tectonic uplift (compressive phase of Ring
 109 et al., (1999)) and/or an increase in aridity causing a global drying of the lake (Owen et al., 2011).

110
 111

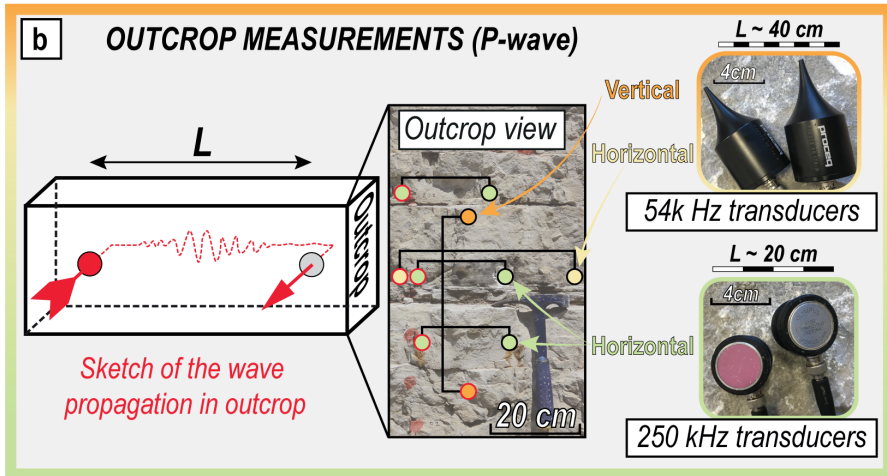


112
 113 **Figure 2.** General framework: (a) Location of Samos Island in the Aegean Sea. (b) Sedimentary basins of
 114 Samos Island and location of the study area (N37°44'21"; E26°53'45"). (c) *GoogleEarth*© view of the
 115 study area showing the studied outcrop and the location of the seismic line. (d) Stratigraphic column
 116 modified after Weidmann et al. (1984) showing the sedimentary infill of Mytilini Basin divided into four
 117 lithostratigraphic formations. The stratigraphic location of our studied section is highlighted in red.
 118

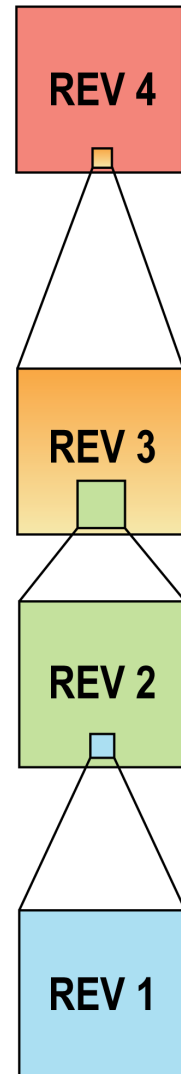
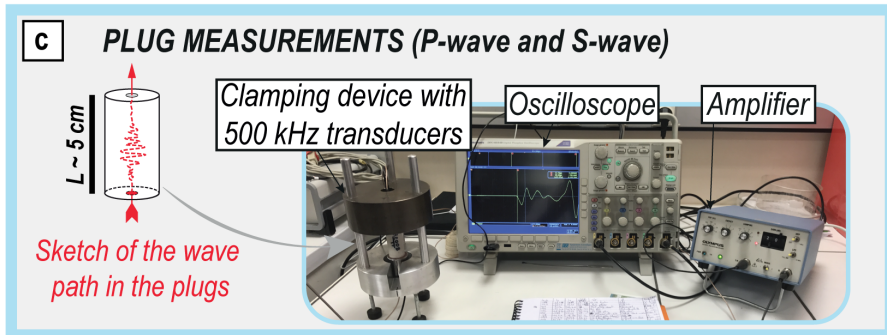
SEISMIC SCALE



OUTCROP SCALE



LABORATORY SCALE



119
120
121
122
123
124
125
126
127
128
129

Figure 3. Applied methodology for this work and corresponding relative evolution of the Representative Elementary Volume (REV): (a) Seismic measurements. On the left, sketches of the refracted wave propagation (SR) produced by a sledgehammer source. The acquisition system (*DAQLINK IV* and geophones) and a field view of the seismic line are indicated on the right. (b) Outcrop measurements. On the left, sketch of the wave propagation in outcrop (with L corresponding to the covered distance). On the middle, outcrop view in reality with examples of the transducer positions during measurements. On the right, 250 kHz and 54 kHz transducers used for P-wave acquisitions. (c) Plug measurements. On the left, sketch of the wave propagation in plug (average length of 5 cm). On the right, acquisition device used for P-wave and S-wave measurements.

130

131 **3. Multi-scale methodology**

132

133 The study site enabled us to acquire acoustic measurements at different scales while keeping a
134 geological control thanks to the outcrop. The frequencies of the different tools used in this work are
135 summarized in Figure 1 and are paired with their wavelengths. A thorough description of this multi-scale
136 geophysical methodology is highlighted in Figure 3. All the acoustic measurements presented in this work
137 were acquired **under dry conditions**. The field campaign was carried out during the end of June 2018, with
138 an average temperature of 25°C and an average humidity of 70 %. Last rainfall occurred 2 days before the
139 measurements, with an amount of water lower than 0.3 mm.

140

141 ***3.1. Outcrop characterization & sampling***

142

143 A sedimentary description of a 40 m thick sedimentary succession was undertaken ('Studied outcrop',
144 Figure 2c) alongside a high-resolution sampling in order to acquire physical properties (one sample every
145 20 cm along a vertical section). Depending on the sample size, plugs were cored with a diameter of 23 mm
146 for 81 samples and 40 mm for 20 samples. Furthermore, panorama pictures aim to highlight outcropping
147 structural features (*e.g.* bedding planes, fractures and faults), showing the structural heterogeneity at outcrop
148 scale (Figure 4).

149

150 ***3.2. Seismic refraction acquisition***

151

152 We carried out a seismic survey that encompasses an 80 m long line ('seismic line', Figure 2c). The
153 sound source is a 4 kg sledge-hammer striking a Teflon plate (central frequency of 100 Hz, Figure 1). Forty-
154 eight geophones with a natural frequency of 10 Hz were regularly spread along a line with a 1 m-spacing
155 and recorded the wave acceleration (Figure 3a). They were covered with sandbags to ensure a good coupling
156 with the ground and limit the ambient noise. Seven shots were done along the seismic line. In order to

157 increase the signal/noise ratio of the recorded waveforms we stacked three times each shot (21 hammer
158 strikes). Refraction processing was then done using Pickwin and Plotrefra software packages from
159 SeisImager, following the processing used by Adelinet et al. (2018). The seismic refraction processing only
160 allowed us to characterize an increase in P-wave velocity with depth. This method provides a wavelength
161 in the range of 20-60 m (decametric wavelength of Figure 1) that offer the opportunity to characterize a
162 large REV (REV 4 of Figure 3).

163

164 *3.3. Outcrop acoustic measurements*

165

166 While the seismic refraction survey was carried out at the top of the outcrop (Figure 2c), P- wave velocities
167 were directly measured on the outcrop surface using a Pundit PL-200 (Jeanne et al., 2012; Matonti et
168 al., 2015) and two types of transducers (Figure 3c). To probe alteration of the outcrop, freshening of the
169 rock surface was done with a hammer. The travel-time (first break) was directly pointed out on the
170 oscillograph and the P-wave velocity is obtained by using the total distance travelled (L of Figure 3). The
171 measurements were obtained with a high vertical sampling (one measurement every 20 cm) and two
172 different spacings between the receiver and transmitters. The 54 kHz transducer were used for measuring
173 P-wave velocity with a spacing of 40 cm between the transducers and two kinds of measurements: i) a
174 vertical transect (orange points of Figure 3b) and ii) a horizontal transect (yellow points of Figure 3b). In
175 parallel, the 250 kHz transducers allowed the measurements of P-wave velocity with a spacing of 20 cm
176 along a horizontal transect (green points of Figure 3b). The peak shape of the 54 kHz transducers made it
177 possible to perform measurements without a coupling gel. However, coupling gel was used for the 250 kHz
178 transducers (Sonctec 54-T04). For the spacing between the transducers, we assume an error of 1 cm. The
179 travel-time error is lower than 5 %. The resulting mean errors are equal to 10 % for the 54 kHz and 250 kHz.
180 These sonic (54 kHz) and ultrasonic (250 kHz) outcrop measurements give us centimetric and millimetric
181 wavelengths (Figure 1) that offer the opportunity to characterize the intermediate length scale (REVs 3 and
182 2 of Figure 3).

183 **3.4. Laboratory measurements**

184

185 Measurements were done in the laboratory on samples cored blocks coming from the outcrop.
186 Porosity and density of 101 were measured with the Archimedes' method (plug mass obtained under three
187 conditions: dry, fluid-saturated and suspended in the saturating-fluid). P- and S- ultrasonic wave velocities
188 were obtained on oven-dry samples (60°C during 48 hours) using 500 kHz transducers connected to an
189 oscilloscope (Figure 3c). The arrival times of P-waves (first break) were directly measured on the
190 oscillograph and divided by the length of samples to calculate P-wave velocities. As indicated by Bailly et
191 al. (2019), the error of this dataset is mainly related to the first break picking (lower than 5 %). Ultrasonic
192 measurements provide millimetric wavelengths that are used to characterize the smaller scale (REV 1 of
193 Figure 3).

194

195 **3.5. Kernel smoothing**

196

197 We applied non-parametric Kernel regressions to smooth the vertical trends of the P-wave
198 velocities acquired at plug and outcrop scales. Then, based on the standard error measured on the smoothed
199 curves, a calculation of the 95 % confidence interval was done using R software.

200

201 **4. Results : Multi-scale dataset, from megascopic scale to microscopic scale**

202

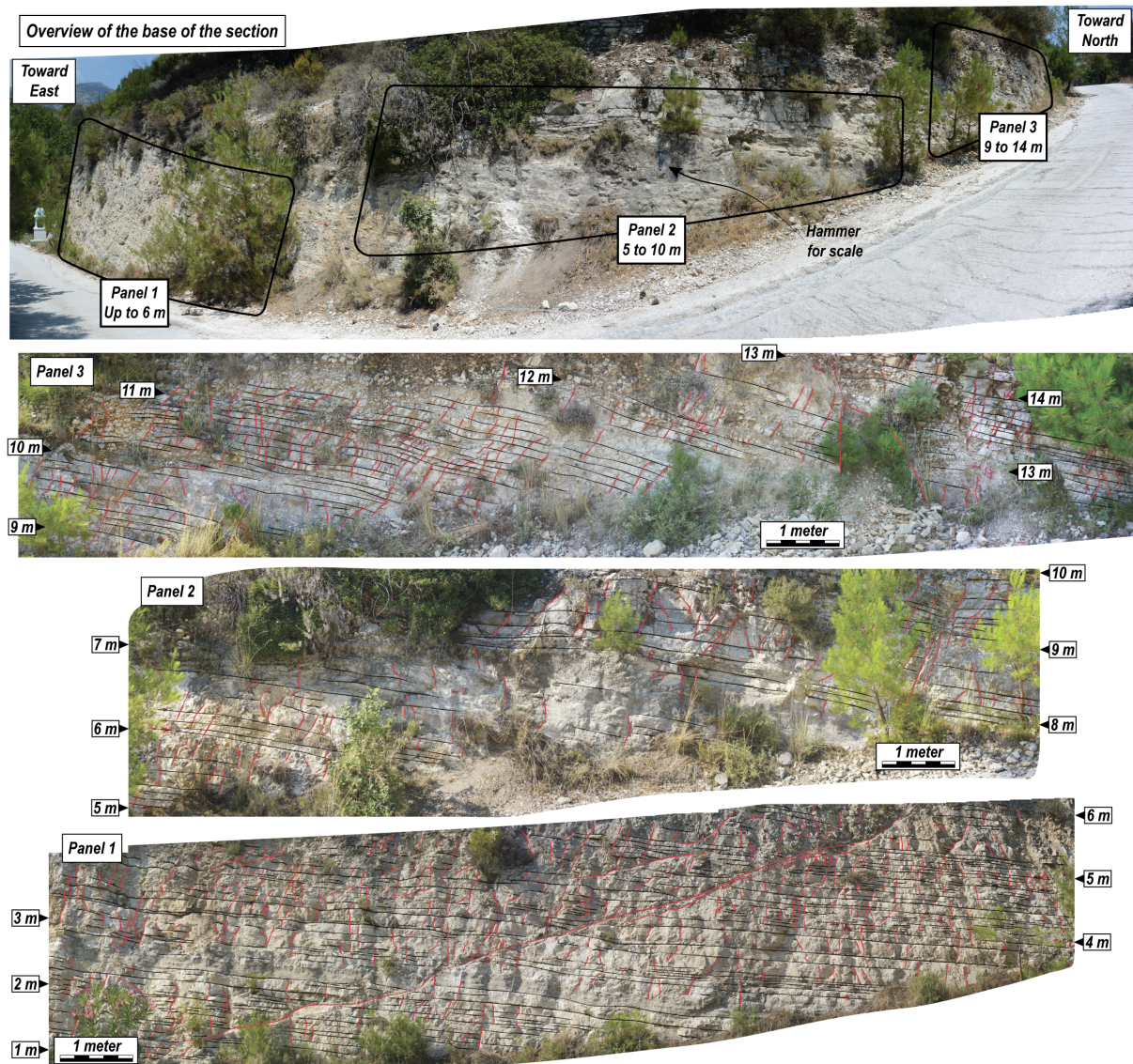
203 **4.1. Structural features at outcrop**

204

205 Figure 4 highlights the studied section and a thorough description of the observed structural
206 features. The mapping of bedding planes (horizontal black lines) outlines a highly stratified pattern that is
207 laterally and vertically persistent (around 3 bedding planes per meter). Furthermore, stratabound and non-
208 stratabound fractures (vertical red lines, around 8 per meter) affect beds, overprinting the horizontal

209 structural features. Finally, a few normal faults are observed (dipping red lines) and crosscut the bedding
210 planes.

211



212 **Figure 4.** Outcrop view highlighting the presence of bedding planes (in dark), fractures and faults (in red).
213

214

215

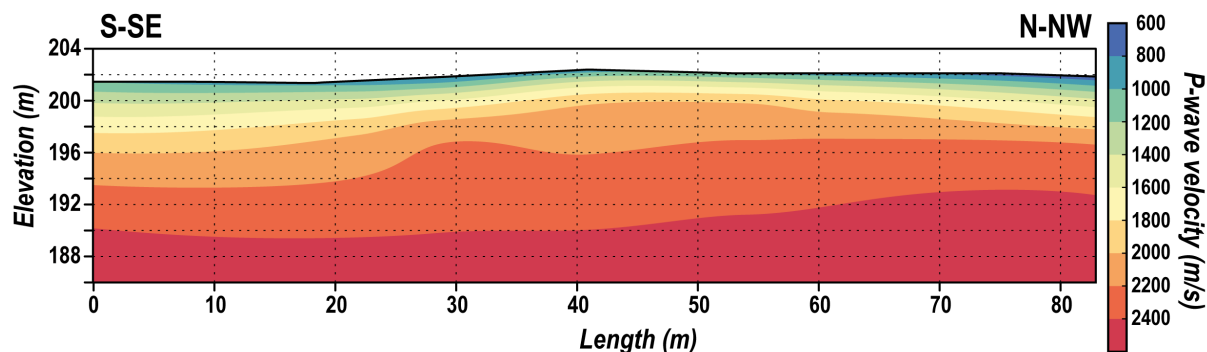
216 *4.2. Seismic refraction dataset, a 2D characterization of elastic properties*

217

218 Figure 5 presents the P-wave velocity profile obtained after inversion (seismic line of Figure 2a).

219 The topography is nearly flat. The first meter of depth correspond to a P-wave velocity equal or lower than

220 1200 m.s⁻¹. Then, the P-wave velocity quickly increases up to 2000 m.s⁻¹ between 2 to 5 meters of depth,
 221 depending on the horizontal location. Finally, P-wave velocity increases more slowly, up to 2400 m.s⁻¹
 222 between 5 to 10 meters depth depending also on the horizontal localization.



223
 224 **Figure 5.** Seismic section obtained after inversion. P-wave velocities are indicated in colors.

225
 226
 227

4.3. Log dataset, a 1D vertical evolution of P-wave velocities

228

229 Figure 6a introduces the sedimentary log described on the field and the associated physical
 230 measurements acquired at multi-scale. The 40 meters thick sedimentary column exhibits mainly carbonate
 231 rocks. The lower part of the sedimentary column shows muddy and grainy carbonates with episodic
 232 exposure surfaces associated with pedogenesis (between 0 and 14 meters). Because of the vegetation cover,
 233 a part of the sedimentary succession has not been studied between 23 and 29 meters; we recognize some
 234 metric beds of grainy carbonates. Then, the top of the sedimentary section highlights again grainy and
 235 muddy carbonates alternating with beds of marls (between 32 and 40 meters). Note that Bailly et al. (2019)
 236 give a more detailed description of the studied outcrop.

237

238 Vertical evolution of porosity acquired in the laboratory are displayed (Figure 6b). From the base
 239 of the outcrop up to 5 m, porosities between 10 % and 25 % are observed and the associated smooth curves
 240 don't show an obvious vertical evolution. Then, between 5 and 14 m, the porosity presents higher values
 241 (up to 35 %) and lower values (down to 5 %) as well as some noticeable vertical fluctuations (metric

242 decrease and increase of porosity). Then, between 24 and 30 m, the smooth curve does not a show
243 significant vertical evolution of porosity (average value of 10-15 %). Between 32 and 36 m, porosity
244 decreases from 25 % down to 5 %. Finally, the last part of the sedimentary column exhibits higher values
245 of porosity centered around 20-25 %.

246

247 Beside the porosity curve, the P-wave velocity acquired on plug, outcrop and seismic scales are
248 displayed. V_{p500} (plug measurements) exhibits ultrasonic P-wave values between 2900 and 5600 $m.s^{-1}$
249 (Figure 6c). Its metric vertical evolution is related to the porosity changes described above: when porosity
250 increases, P-wave velocity decreases and *vice versa* (see also Figure 7b).

251

252 V_{p250} (*in-situ* horizontal outcrop measurements) shows P-wave values between 1000 and
253 5000 $m.s^{-1}$ (Figure 6d), its fluctuations are higher than V_{p500} . From the base of the outcrop up to 14 m, the
254 smoothed curve associated with V_{p250} presents metric fluctuations of P-wave velocity with values centered
255 around 2000 and 4000 $m.s^{-1}$ with values up to 4500 $m.s^{-1}$ between 10 and 12 meters. Later, between 24 and
256 30 meters, V_{p250} presents obvious vertical fluctuations that were not recorded with V_{p500} . Between 32 and
257 40 meters, V_{p250} highlights meter-scale fluctuations with values up to 5000 $m.s^{-1}$ and down to 1000 $m.s^{-1}$.

258

259 V_{p54H} (horizontal *in-situ* outcrop measurements) presents P-wave values between 500 and
260 4500 $m.s^{-1}$ (Figure 6e). For the first part of the sedimentary column (0 to 14 meters), most of the vertical
261 fluctuations of V_{p54H} are similar to V_{p250} , showing P-wave velocity values centered around 2000 and
262 3000 $m.s^{-1}$. Then, between 24 and 30 meters, the fluctuations of V_{p54H} mimic V_{p250} with lower P-wave
263 velocity values (500 to 4000 $m.s^{-1}$). Between 32 and 35 meters, V_{p54H} presents a more chaotic vertical
264 fluctuation not similar to V_{p250} , with P-wave velocity values comprised between 500 and 3500 $m.s^{-1}$.

265

266 V_{p54V} (vertical *in-situ* outcrop measurements) presents P-wave values between 1000 and
267 3500 $m.s^{-1}$ (Figure 6f). Its vertical fluctuations are partly similar to V_{p54H} (e.g. between 3 and 6 meters,

268 around 25 and 28 meters, between 32 and 34 meters) but present a more chaotic fluctuation in the remaining
269 part of the sedimentary column.

270

271 Finally, V_{p100} (seismic data) is also presented for comparison of the overall P-wave velocity dataset
272 on a vertical way (Figure 6g). Because of the vertical resolution, the lower part of the sedimentary column
273 is not imaged (*non-visible zone* in Figure 6g). As previously showed in Figure 5, the highest P-wave velocity
274 value of V_{p100} is about $2400 \text{ m}\cdot\text{s}^{-1}$, reached between 25 and 28 meters. Then, between 28 and 37 meters,
275 V_{p100} decreases linearly down to $2000 \text{ m}\cdot\text{s}^{-1}$. At the top of the sedimentary column (37 to 40 meters), V_{p100}
276 decreases drastically down to $800 \text{ m}\cdot\text{s}^{-1}$.

GEOLOGICAL DATASET

LABORATORY SCALE

GEOPHYSICAL DATASET

OUTCROP SCALE

SEISMIC SCALE

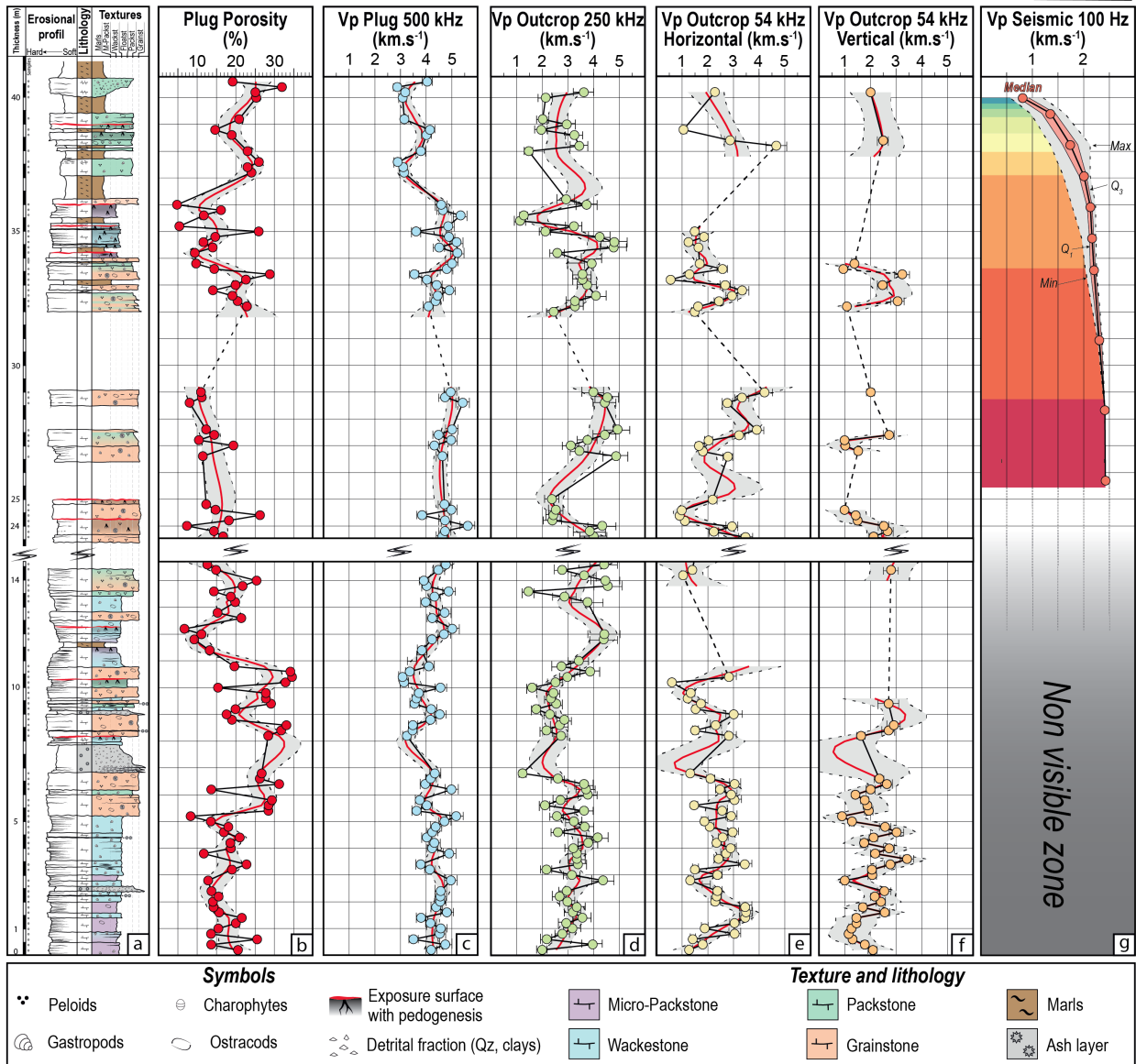


Figure 6. (a) Sedimentary log compared with vertical variations of (b) plug porosity and P-wave velocity acquired at (c) laboratory (500 kHz), (d) (e) and (f) outcrop (250 and 54 kHz) and (g) seismic (100 Hz) frequencies. Smooth curves with their 95 % confidence interval are also indicated in order to describe the vertical variations of each dataset.

277
278
279
280
281
282

283

284

285

286

287 **4.4. Porosity-ultrasonic velocity relationship at plug scale**

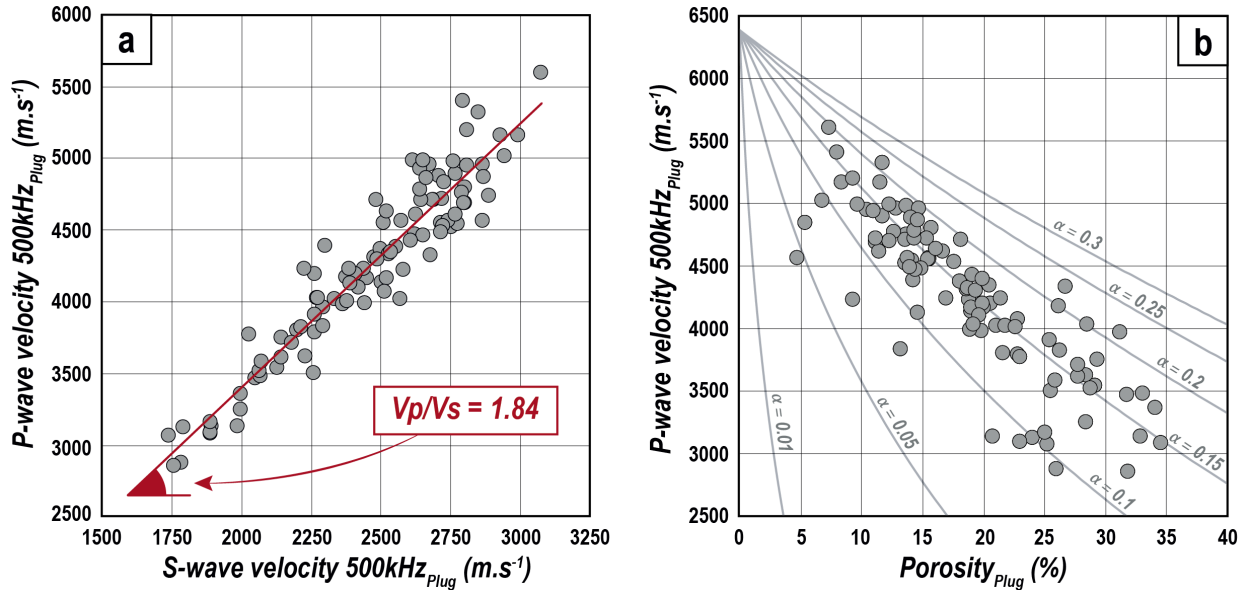
288

289 Figure 7a shows the P- and S-wave velocities acquired on plugs. V_{p500} values range between 2800
290 and 5600 m.s^{-1} , while V_{s500} values range between 1600 and 3100 m.s^{-1} . The V_{p500} versus V_{s500} plot exhibits
291 a good linear trend ($R^2=0.89$) that indicates a V_p/V_s ratio equal to 1.84, consistent for carbonate rocks
292 (assuming a Poisson ratio equal to the one of pure calcite, a ratio of $V_p/V_s=1.91$ is expected, Mavko et al.,
293 2009).

294

295 Figure 7b exhibits V_{p500} versus porosity. It shows a clear decrease of velocities with an increase of
296 porosity. For explaining the scattering of velocities for a given porosity, we use the analytical expressions
297 of David and Zimmerman (2011b) that aims to compute the effective elastic properties of an isotropic solid
298 containing randomly oriented spheroidal pores. Thanks to this DEM model, we compute the aspect ratio
299 ($0.01 < \alpha < 0.3$, ratio between the longer and the shorter length of an ellipse) embedded in a pure calcite
300 medium ($V_{p\text{Calcite}} = 6400 \text{ m.s}^{-1}$). The resulting mean pore aspect ratio is about $\alpha = 0.16$ ($\sigma = 0.04$), shows a
301 minimum of 0.04 and a maximum of 0.25. These results about the aspect ratio in carbonate rocks are
302 consistent with previous studies (e.g. Fournier et al. (2018); Regnet et al. (2019a)).

303



304
 305 **Figure 7.** Plug data: (a) V_{p500} versus V_{S500} and associated trend (red line). (b) V_{p500} versus porosity.
 306 Curves of constant aspect ratio of pores are indicated for a pure calcite matrix.

307

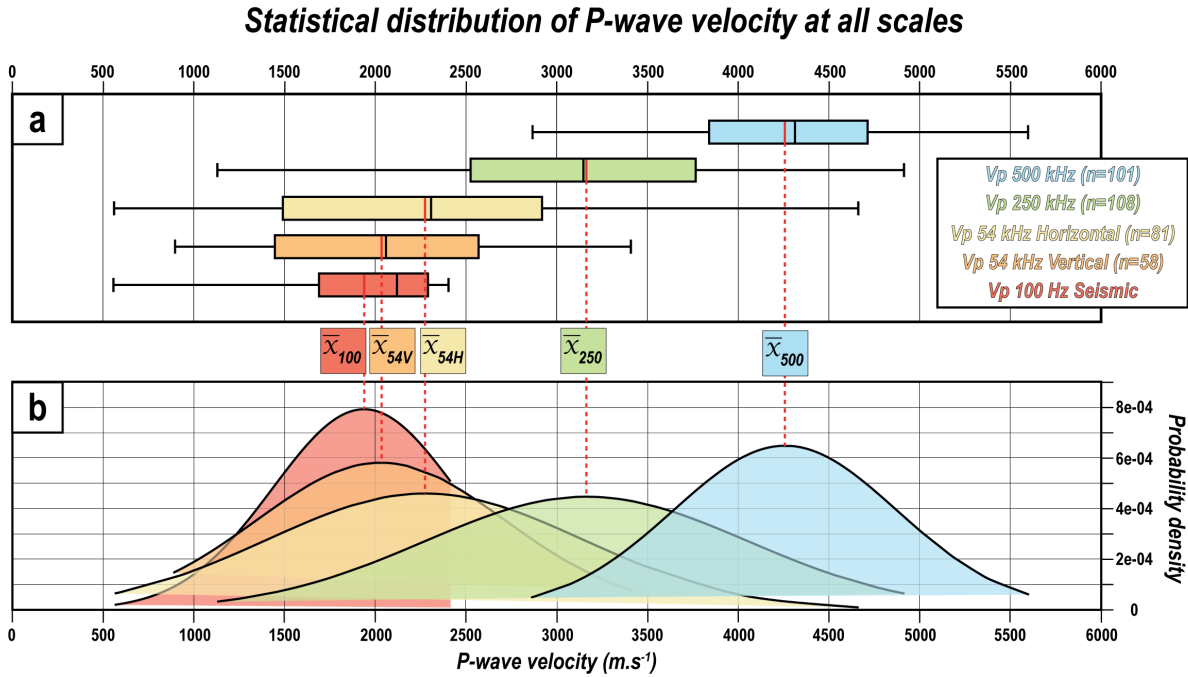
308 **4.5. Statistical distribution of the multi-scale P-wave velocity**

309

310 The boxplots, of each P-wave velocity dataset acquired in this work, are shown in Figure 8a. For
 311 V_{p500} , half of the dataset is comprised between 3800 and 4700 $m.s^{-1}$, with a median of about 4300 $m.s^{-1}$.
 312 Then, V_{p250} displays lower values of velocity, with half of this dataset comprised between 2500 and 3800
 313 $m.s^{-1}$, and a median of 3200 $m.s^{-1}$. The interquartile of V_{p54H} is comprised between values of 1500 and 2900
 314 $m.s^{-1}$, and partly overlaps V_{p250} with a median equal to 2300 $m.s^{-1}$. V_{p54V} completely overlaps V_{p54H} , with
 315 half of its values comprised between 1500 and 2600 $m.s^{-1}$, and a median equal to 2000 $m.s^{-1}$. Finally, half
 316 of the values of V_{p100} are comprised between 1700 and 2300 $m.s^{-1}$, with a median of 2200 $m.s^{-1}$.

317 The normal laws of each dataset are shown in Figure 8b. Data acquired in the laboratory and outcrop
 318 exhibit a nearly symmetrical distribution (median \approx mean). Contrarily, V_{p100} shows an asymmetric
 319 distribution, (median $<$ mean). It has to be noted that V_{p500} , V_{p54V} and V_{p100} show less scattering than V_{p250}
 320 and V_{p54H} (flattening of the curves).

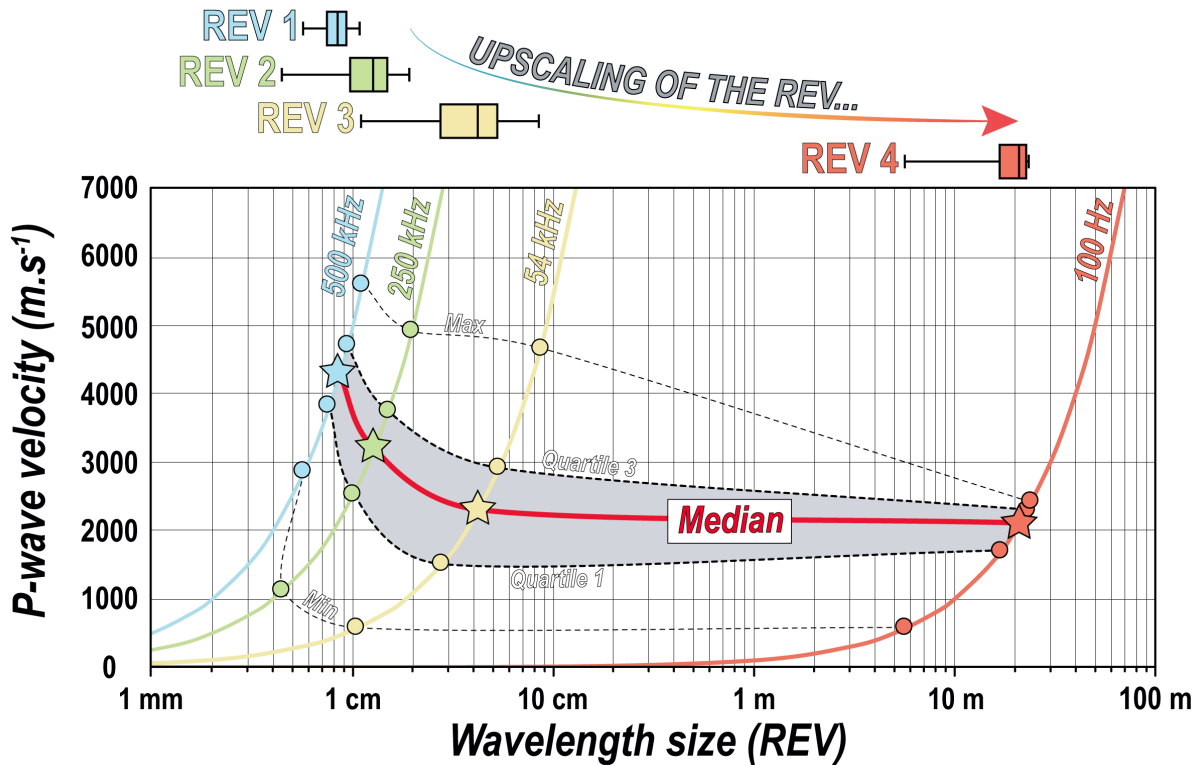
321



322
 323 **Figure 8.** Statistical distribution of P-wave velocities at all scales. (a) Boxplots of each dataset with mean
 324 indicated. (b) Normal laws of each data set, showing the difference of mean and standard deviation.

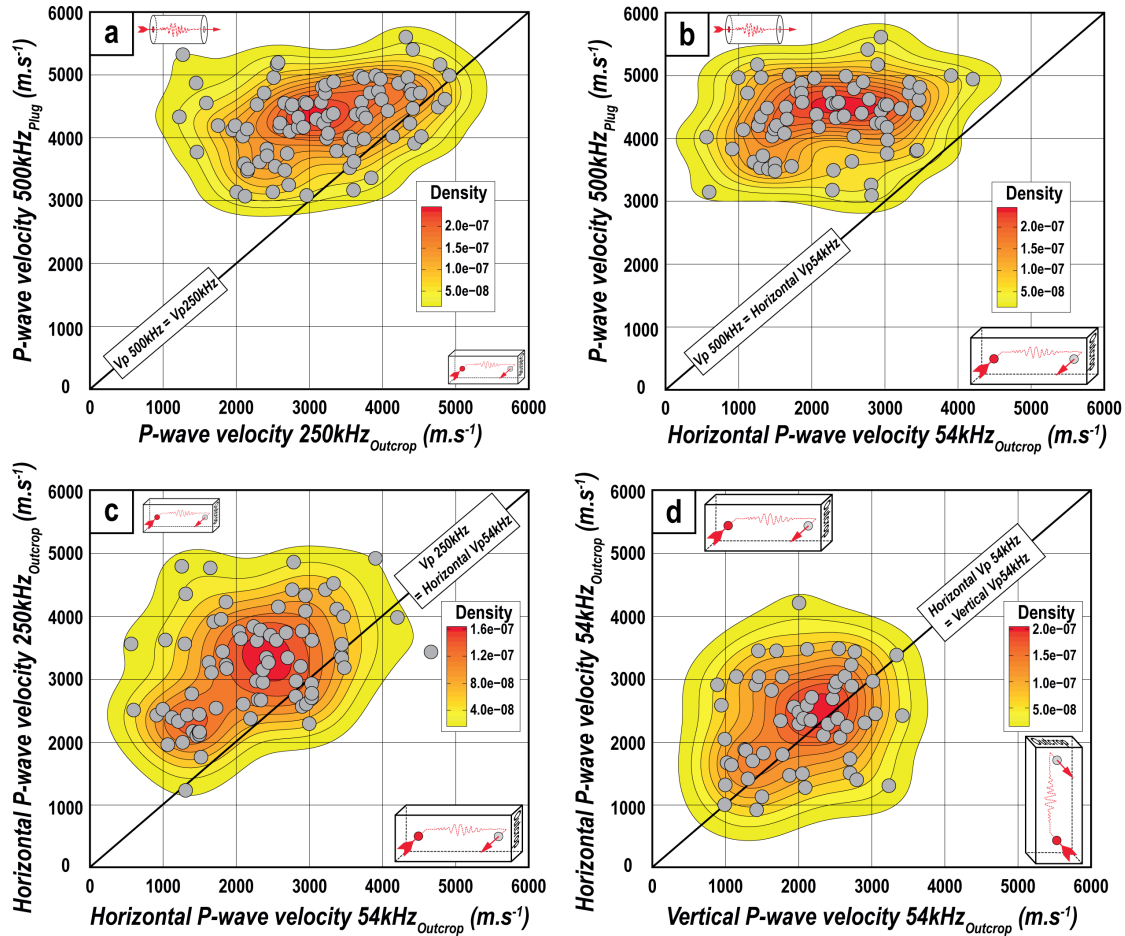
325
 326 Figure 9 summarizes the descriptive statistics of P-wave velocity of each dataset (Figure 8a) *versus*
 327 their corresponding wavelength. In addition, the four curves of constant frequency induced by the different
 328 geophysical tools are plotted. An overall decrease of P-wave velocity is observed, from ultrasonic to seismic
 329 frequency (Figure 9). This shift of P-wave velocity is particularly well-defined by the interquartile domain
 330 and the median of each dataset. The main decline of the P-wave velocity is observed between V_{p500} and
 331 V_{p54H} , with a decrease of about $2000 m \cdot s^{-1}$, associated with an increase of the wavelength size, from 6-
 332 10 mm for λ_{500} to 2-6 cm for λ_{54} . Then, between V_{p54} and V_{p100} , the P-wave velocity decreases to a lesser
 333 extent (decrease of $200 m \cdot s^{-1}$) despite that, the associated wavelength increases from 2-6 cm for λ_{54} to ~ 20 m
 334 for λ_{100} . This last result (comparison between V_{p54} and V_{p100}) suggests that the elastic properties
 335 characterized at a sonic frequency are representative of elastic properties acquired at seismic frequency, at
 336 least for the study site that we investigate.

337



338
 339 **Figure 9.** P-wave velocities of four datasets versus wavelength size (REV). Only the descriptive statistics
 340 of P-wave velocity and wavelength are displayed. The grey area corresponds to the interquartile range and
 341 the red curve shows the median. Curves of constant frequency are also indicated. Boxplots showing the
 342 evolution of the wavelength with scale are displayed on the top.

343
 344 The descriptive statistics of P-wave velocity of each dataset can be also investigated through
 345 probability density maps (PDM, Figure 10). In Figure 10a, most of the dataset exhibits V_{p500} higher than
 346 V_{p250} even if a few data points are located close to the line of equality. The highest values of PDM indicate
 347 V_{p500} between 4000 and 5000 $m.s^{-1}$ while V_{p250} scatters between 2000 and 4500 $m.s^{-1}$. This observation is
 348 further reinforced by Figure 10b, showing V_{p500} always higher than V_{p54H} . Again the highest values of
 349 PDM suggests V_{p500} between 4000 and 5000 $m.s^{-1}$ while V_{p54} scatters between 1000 and 3500 $m.s^{-1}$. Figure
 350 10a,b clearly shows that there is no direct relationship between plug and outcrop measurements, an
 351 observation that points to a scale effect. Indeed, outcrop measurements take into account greater scales of
 352 heterogeneities than plug measurements, including the impact of interfaces at the outcrop scale (e.g. cracks,
 353 fractures, Figure 4).



354
 355 **Figure 10.** Comparison of P-wave data acquired at the outcrop and laboratory with probability density
 356 maps (PDM). Line of equality between datasets are also indicated. (a) V_{p500} versus V_{p250} . (b) V_{p500} versus
 357 V_{p54H} . (c) V_{p250} versus V_{p54H} . (d) V_{p54H} versus V_{p54V} .

358
 359 Further findings at the outcrop scale are highlighted with the Figure 10c which compare V_{p250} with
 360 V_{p54} . In this plot, the major part of the dataset exhibits V_{p250} higher than V_{p54H} with a few data points located
 361 close to the line of equality. Moreover, despite the scattering of the dataset, the PDM shows a linear trend
 362 that mimics the line of equality, suggesting that V_{p250} and V_{p54H} are sensitive to the same features. This
 363 result goes hand in hand with the previous observations made in Figure 10a, b, cracks and fractures affect
 364 mainly the elastic properties of outcrop measurements. Finally, the Figure 10d compares V_{p54H} with V_{p54V}
 365 acquired at outcrop on the same locality. Despite the scattering of the dataset, the highest values of PDM
 366 are around the line of equality, indicating an almost elastic isotropy. This finding denotes that the defects
 367 affecting the elastic properties of outcrop scale are almost randomly distributed.

368 **5. Discussion: Upscaling of physical properties in carbonates**

369

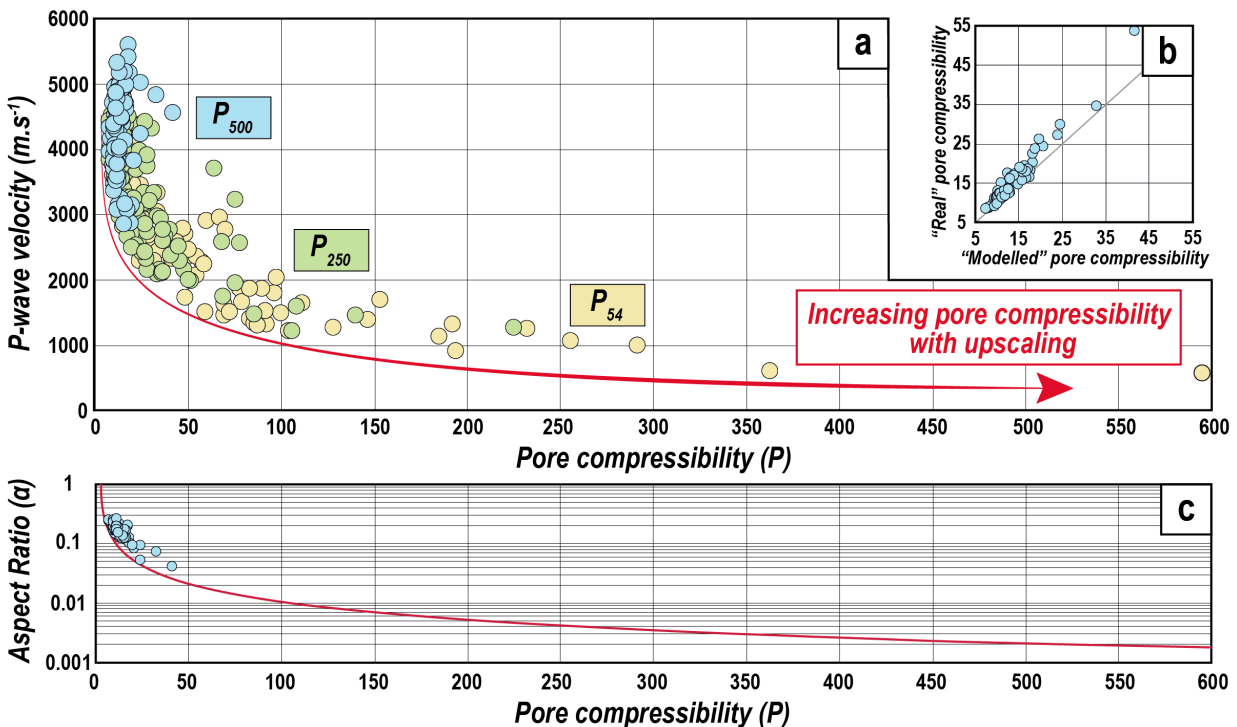
370 **5.1. Insight through the pore compressibility evolution from plug scale to outcrop scale**

371

372 We use a simple effective medium model to determine the evolution of the pore compressibility
 373 with scale: from plug to outcrop, assuming a homogeneous, isotropic and dry medium. According to the
 374 Mori-Tanaka scheme, Benveniste (1987) shows that the effective bulk modulus, K_{eff} , is related to the
 375 porosity, Φ , the bulk modulus of the pore-free matrix, *i.e.* the bulk modulus of the calcite ($K_0 = 71$ GPa)
 376 and the pore compressibility (P) is normalized to the compliance of a spherical pore (David and
 377 Zimmerman, 2011a):

$$\frac{K_0}{K_{\text{eff}}} = 1 + \frac{\Phi}{(1 - \Phi)} P(v_0). \quad (1)$$

378



379

380 **Figure 11.** Pore compressibility control on P-wave velocity. (a) P-wave velocity versus pore
 381 compressibility for three datasets calculated for a Poisson ratio of 0.29. (b) Real versus modelled pore
 382 compressibility for ultrasonic laboratory data. (c) Relationship between aspect ratio and pore
 383 compressibility for a calcite medium (red line calculated for an equivalent ellipsoidal pore). The blue dots
 384 represent the aspect ratio determined for spheroidal pores at the plug scale (Figure 7b).

385 The effective bulk (K_{eff}) and shear (G_{eff}) moduli are related given by the following set of equations
 386 (2) and (3):

$$V_p^2 = \frac{K_{\text{eff}} + \frac{4}{3}G_{\text{eff}}}{\rho_b}, \quad (2)$$

$$V_s^2 = \frac{G_{\text{eff}}}{\rho_b}, \quad (3)$$

387 where ρ_b is the density of the studied medium. At the plug scale, V_p , V_s and Φ are measured. Using
 388 equations (2) and (3) one can compute the effective bulk modulus, and then compute the pore
 389 compressibility at plug scale (P_{500}), using equation (1). Results are plotted in Figure 11a (dots in blue) and
 390 show values for P_{500} between 12 and 17.

391
 392 Then, for computing P at outcrop scale without knowing V_s , we make the approximation that the
 393 Poisson ratio (ν) obtained at plug scale is constant whatever the scale. At the plug scale, $V_p/V_s = 1.84$,
 394 leading to ν_{eff} equal to 0.29, a value close to the one of a pure calcite mineral ($\nu_{\text{Calcite}} = 0.31$). Equations (2)
 395 and (3) can be combined to get :

$$K_{\text{eff}} = \frac{V_p^2 \rho_b}{1 + 4 \left(\frac{1 - 2\nu_{\text{eff}}}{2 + 2\nu_{\text{eff}}} \right)} \quad (4)$$

396 At the plug scale, the comparison of the “real” pore compressibility P (*i.e.* the one calculated by using V_p
 397 and V_s data) and the one calculated under the assumption that ν_{eff} is constant and equal to 0.29 (“Modelled
 398 pore compressibility” in Figure 11b) aims to show that the “modelled” P is slightly underestimated, *i.e.*
 399 under the assumption that ν_{eff} is constant, pores appear slightly stiffer than they are in reality (Figure 11b).
 400 We also assume that there is no significant porosity change between the plug and the outcrop scale, which
 401 is a valid approximation, as the porosity of the plugs are in the range 10-30 % and at larger scale the
 402 additional porosity due to the cracks and fractures is expected to be ≤ 3 %. Thus, we can use the set of
 403 equations (1) and (4) to compute the pore compressibility at an outcrop.

404

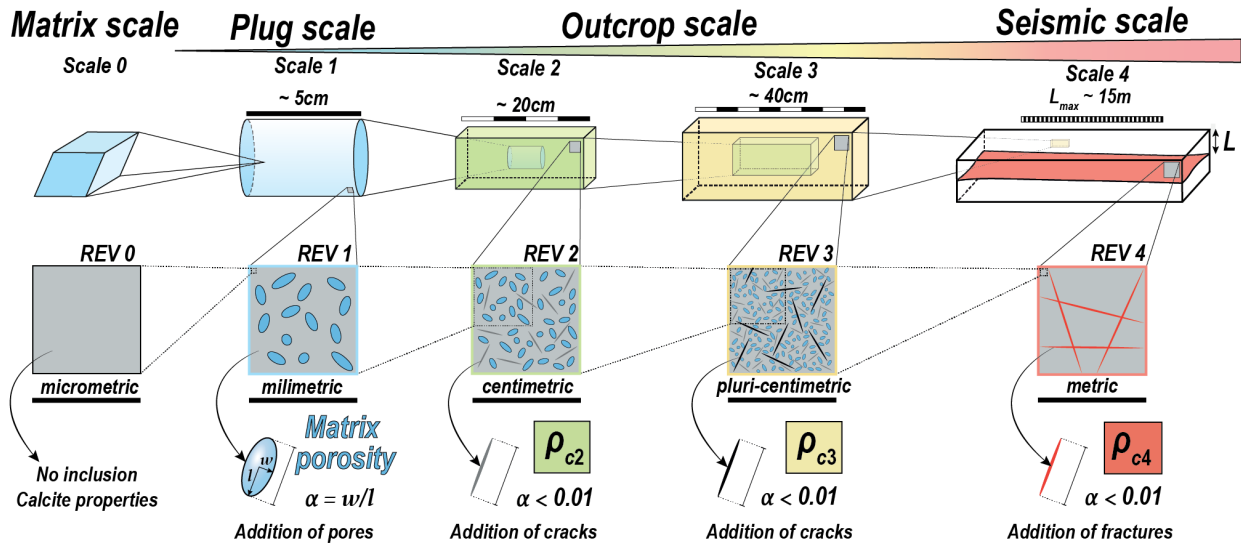
405 The P-wave velocity acquired at plug and outcrop are plotted *versus* their associated pore
406 compressibility (Figure 11a). Results show that there is an increase of the pore compressibility with
407 upscaling, implying a softening of the porous network from laboratory scale to outcrop scale (porous
408 medium containing more and more compressible/soft pores, *e.g.* cracks). Indeed, from V_{p500} to V_{p54} , P
409 increases and can reach values up to 600. The Figure 11a shows that for P-wave values range between 1000
410 and 2000 $\text{m}\cdot\text{s}^{-1}$, the associated P values tend to be higher than 50-100 (threshold value). According to David
411 and Zimmerman (2011a), we can relate P with the aspect ratio (α) of an equivalent ellipsoidal pore. We use
412 their asymptotic approximations to compute an “effective” aspect ratio for a given P (red curve of
413 Figure 11c). For plug data, the equivalent aspect ratios calculated using the model of David and Zimmerman
414 (2011a) are slightly lower than the effective aspect ratios previously obtained with DEM modeling (David
415 and Zimmerman, 2011b). Comparing the threshold value observed on Figure 11A (P around 50-100) with
416 the Figure 11C allows us to conclude that upscaling from the plug to outcrop scale is characterized by an
417 addition of very soft pores ($\alpha < 0.01$, cracks). These very soft pores may be linked with the structural
418 features observed on the outcrop (Figure 4).

419

420 ***5.2. Upscaling modeling of elastic properties, from ultrasonic to seismic frequencies***

421

422 As stated before, the upscaling of elastic properties in carbonates need to take into account different
423 geological scales (Figure 1). Using an effective medium model, it is possible to model the evolution of P-
424 wave velocity with scale, as described by the Figure 12.



426

427 **Figure 12.** Modeling of the elastic properties at different scales by adding pores ($0.01 < \alpha < 0.3$) and
 428 cracks/fractures ($\alpha < 0.01$) of different sizes relating to the REV.

429

430

431 At the matrix scale, the elastic properties of the medium are equal to the one of a pure calcite
 432 mineral ($K_0 = K_{\text{calcite}} = 71 \text{ GPa}$, $G_0 = G_{\text{calcite}} = 30 \text{ GPa}$; Mavko et al., 2009). Then, at plug scale, the elastic
 433 properties K_1 , G_1 are assumed to be the one of a calcite matrix containing spheroidal pores of a given
 434 equivalent aspect ratio. These elastic properties are computed employing the asymptotic expressions given
 435 by David and Zimmerman (2011b). In Figure 7b, the obtained results show that most of the plug-scale data
 436 corresponds to an aspect ratio between 0.1 and 0.2, a range close to the reference of carbonates ($\alpha_{\text{ref}} \sim 0.15$)
 437 given by Xu and Payne (2009) and Fournier et al. (2018) who also used DEM modeling. This first step of
 438 inverting P-wave velocity and porosity data in terms of equivalent pore aspect ratio is now widely used in
 439 the literature (e.g. Baechle et al., 2008; Fournier et al., 2011, 2014, 2018; Regnet et al., 2019a; Xu and
 440 Payne, 2009). It aims to explain the scattering of P-wave velocity for a given porosity and is of crucial
 441 importance for reducing the uncertainties in inverting and interpreting seismic data (Eberli et al., 2003).
 442 Nevertheless, the aspect ratio obtained, at plug scale, are representative of a small REV containing
 443 millimetric pores, and are not necessarily equal to the one of a larger volume (Figures 8, 9, 10 and 11).

443

444 At the outcrop scale, one should take into account a second family of inclusions, characterized by
 445 a low aspect ratio ($\alpha < 0.01$, Figure 11) related to the cracks/fractures observed in the field (Figure 4). We
 446 can use the crack density (ρ_c) defined by Walsh (1965) for quantifying the amount of circular cracks at
 447 different scales (Figure 12, equation 5):

$$\rho_c = \frac{1}{V} \sum_{i=1}^n c_i^3, \quad (5)$$

448 ρ_c is the crack density for n cracks of radius c in a volume V . Following David and Zimmerman (2011b),
 449 asymptotic solutions for the DEM in the case of crack-like pores ($\alpha < 0.01$) give us expressions of the
 450 effective moduli K and G as explicit functions of ρ_c :

$$\frac{K_{i+1}}{K_i} = \frac{(1 - 2\nu_i) e^{-\frac{16}{9}\rho_c}}{1 - 2\nu_i e^{-\frac{8}{5}\rho_c}}, \quad (6)$$

$$\frac{G_{i+1}}{G_i} = \frac{(1 + \nu_i) e^{-\frac{16}{9}\rho_c}}{1 + \nu_i e^{-\frac{8}{5}\rho_c}}, \quad (7)$$

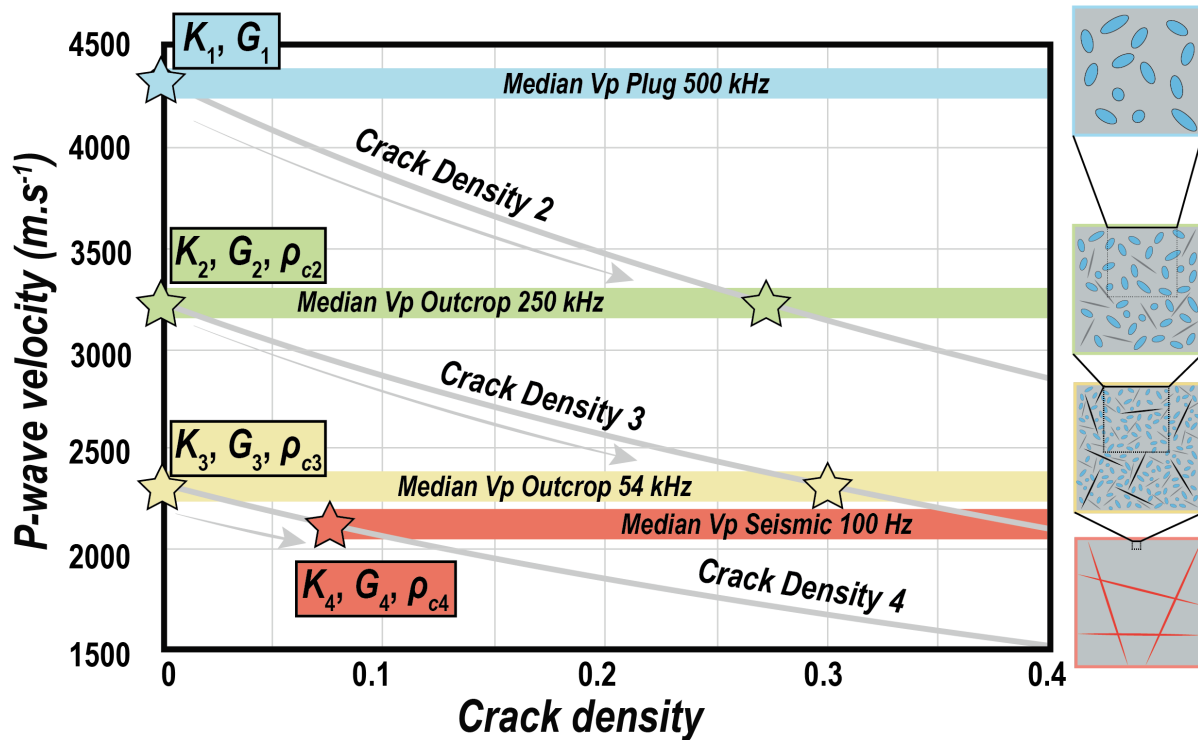
451 where K_i , G_i and ν_i are the effective elastic moduli of the lower scale ($i=1, 2, 3$). Note that in the set of
 452 equations 6 and 7, we remove the previous assumption of constant Poisson ratio that was only used to
 453 compute pore compressibilities. In the following, the plug scale (V_{p500}) corresponds to the scale 1 (REV 1
 454 of Figure 12), the first outcrop scale (V_{p250}) corresponds to the scale 2 (REV 2 of Figure 12), the second
 455 outcrop scale (V_{p54}) corresponds to the scale 3 (REV 3 of Figure 12) and the seismic scale (V_{p100})
 456 corresponds to the scale 4. As an exemple, for the upscaling from scale 1 to scale 2: K_1 and G_1 are taken as
 457 the median value deduced from the data obtained on plugs (V_{p500}); K_2 is taken as the median value deduced
 458 from the data obtained on outcrop (V_{p250}); then, using equation 6 and 7, one can compute the crack
 459 density ρ_{c2} (Figure 13).

460

461 Figure 13 shows the calculated ρ_{ci} between scales based on the median values of P-wave velocities
 462 obtained for each dataset. First, the decrease of P-wave velocity with upscaling from scale 1 to scale 2, is

463 associated with a ρ_{c2} value of 0.27 related to the presence of cracks with a size ≤ 2 cm (λ_{250} , Figure 9). The
464 resulting medium, REV2 of Figure 12, thus presents cracks ≤ 2 cm embedded within a porous carbonate
465 with spheroidal pores ≤ 1 cm characterized by an aspect ratio around 0.15 (α_{ref}).
466

467 Then, the P-wave velocity decreases again with upscaling between V_{p250} and V_{p54} . The transition
468 from scale 2 to scale 3 is linked with an addition of another crack density $\rho_{c3} = 0.3$ related to the presence
469 of cracks with size ≤ 6 cm (λ_{54} , Figure 9). The resulting medium, REV 3 of Figure 12, thus contains two
470 different scales of crack density, ρ_{c2} and ρ_{c3} , embedded in a porous medium. Finally, passing from scale 3
471 to scale 4 implies again an addition of another crack density ($\rho_{c4} = 0.07$) related to cracks/fractures of a size
472 ≤ 20 m (λ_{100} , Figure 9). The resulting REV 4 includes three different scales of cracks, ρ_{c2} , ρ_{c3} and ρ_{c4} ,
473 embedded within a matrix porosity characterized by pores with an equivalent pore aspect ratio equal to
474 0.15. This multi-scale concept aims to explain the overall decrease of P-wave velocity from plug to seismic
475 scale by taking into account different scales of heterogeneities, corresponding to different REV's, that have
476 geological and physical significances (*i.e.* pores, cracks and fractures). It is therefore of importance for
477 understanding of the physical properties of subsurface reservoirs (*i.e.* fractured carbonate reservoirs).



478
479 **Figure 13.** P-wave velocity versus computed crack densities for the median of each acoustic dataset.

480
481 **5.3. From elasticity to reservoir properties of carbonates, implications of the crack porosity**

482
483 As shown by several authors, reservoir properties (like porosity and permeability) are controlled
484 by different factors (*e.g.* pore types and sizes) regarding the scale of investigation (Corbett, 2009; Haldorsen
485 and Lake, 1984; Nordahl, 2004; Ringrose et al., 2008; Ringrose and Bentley, 2015). The multi-scale elastic
486 properties obtained in this work are similar to what is found in the literature. At the lower scales of
487 investigation (microscopic and macroscopic scales of Figure 1), the microstructure controls the physical
488 properties of carbonates (Anselmetti and Eberli, 1993; Regnet et al., 2019b). Indeed, the microstructures
489 present a huge diversity of sedimentary textures that may be modified by diagenetic processes, implying an
490 important heterogeneity of their physical properties. DEM modeling shows that most of the dataset indicates
491 an equivalent pore aspect ratio range equal to the reference value of carbonates ($\alpha_{ref} = 0.15$), despite samples
492 present a high variability of microstructures. Then, for higher scales of investigation, the presence of large
493 scale structural features impact the elastic properties (Figure 4). Again, using DEM modeling, we invert the

494 P-wave velocity evolution with scale in terms of crack density, highlighting that the different scales are
 495 impacted by structural features (Figures 12 & 13). Furthermore, based on the assumption that the cracks
 496 and fractures have an aspect ratio equal to 10^{-3} (Figure 11) we can compute the crack porosity thanks to the
 497 following equation (David and Zimmerman, 2011b):

$$\Phi_{crack} = \frac{4}{3} \pi \rho_c \alpha_{crack}, \quad (8)$$

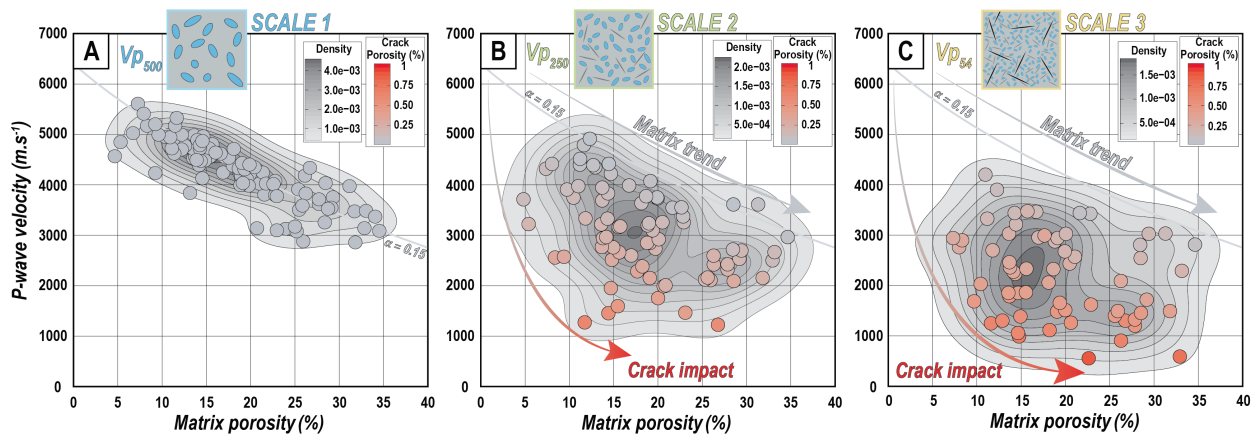
498 where Φ_{crack} is the computed crack porosity, ρ_c is the crack density and α_{crack} is the crack aspect ratio (here
 499 assumed to be equal to 10^{-3}). Using equation (8), with the values of crack density previously obtained,
 500 (Figure 13) give us a total amount of megascopic crack/fracture porosity equal to 0,27 % ($\Phi_{crack2} + \Phi_{crack3}$
 501 + Φ_{crack4}). This value is close to the one recently obtained by Panza et al. (2019), who used a stochastic
 502 approach (Discrete Fracture Network modeling based on field structural analysis) to compute the fracture
 503 porosity of a 1 m^3 block of tight carbonate (mean $\Phi_{crack} = 0.3 \%$).

504

505 The estimation of the crack-fracture porosity done above is computed using the median V_p value
 506 for each dataset. We can also compute “local” crack porosity for scales 2 and 3. For example for scale 2,
 507 ($i=1$, in equation 6 and 7) we can use the plug values for K_1 , and K_2 from local log measurement (instead
 508 of using the median value of the dataset), then we can compute local crack/fracture porosity. Figure 14
 509 shows the dataset for scales 1, 2 and 3 in a velocity-porosity plot. As expected before with the Figure 10a, b,
 510 the primary control of matrix porosity on the P-wave velocity tends to be lost with upscaling (Figure 14).
 511 Indeed, for the scale 2, almost all V_{p250} values are lower than the $\alpha_{ref=0.15}$ curve (Figure 14b). In the upper
 512 part of the PDM, most of the dataset presents Φ_{crack} values lower than 0,1 % and tends to mimic the matrix
 513 trend. In the lower part of the PDM, the scattering increases and is associated with an increasing Φ_{crack} (up
 514 to 0,6 %). For the scale 3, all V_{p54} values are lower than the $\alpha_{ref=0.15}$ curve (Figure 14c). The highest velocity
 515 values shown in the PDM do not highlight any links between P-wave velocity and porosity. Furthermore,
 516 for medium porosity (between 10 and 20 %), the Figure 14c shows a huge fluctuation of P-wave velocity
 517 (between 3500 and 1000 m.s^{-1}) associated with an increase in Φ_{crack} (from 0,1 to 0,6 %). The progressive

518 scattering of the velocity-porosity data, in Figure 14b, c, shows that the “matrix-porosity” control does not
 519 affect the elastic properties anymore with upscaling from laboratory scale to outcrop scale.

520



521
 522 **Figure 14.** Impact of the crack density/porosity on the elastic properties. (a) P-wave velocity (500 kHz)
 523 versus matrix porosity (i.e. plug porosity). The grey dots indicate the data obtained at plug scale that follow
 524 the curve of equivalent $\alpha = 0.15$ without crack porosity. (b) P-wave velocity (250 kHz) versus matrix
 525 porosity with curves of constant crack porosity. The colored dots indicates the inverted crack porosity value
 526 for all the data (Φ_{crack2}). (c) P-wave velocity (54 kHz) versus matrix porosity with curves of constant crack
 527 porosity. The colored dots indicates the inverted crack porosity value for all the data ($\Phi_{crack2} + \Phi_{crack3}$).
 528 (Grey dots = no crack porosity; red = crack porosity of 1 %).

529

530

531

532

533

5.4. How to define the elastic properties of carbonates at different scales?

534

535 Figure 15 summarizes the upscaling of the wavelength size, P-wave velocity and porosity and their
 536 associated major controlling factors (porosity of the matrix, cracks and fractures). In order to be
 537 representative of a medium, the geological interpretation of an elastic measurement needs to be within the
 538 constraints of the REV size (λ , Figure 15a) which depends on i) the tool frequency (f) and ii) the P-wave
 539 velocity (v) using the well-known relationship : $\lambda=v/f$. Following the theory of homogenization, the upper
 540 limit size of an elastic REV has to be lower than the wavelength size induced by the used geophysical tool.
 541 Conversely, by analogy with seismic investigation, the lower limit of an elastic REV has to be higher than
 542 the quarter wavelength size (Sheriff and Geldart, 1995). Indeed, this resolution corresponds to the minimum

543 interval between two interfaces to be seen as two separate objects and not a single one, it therefore can be
544 used as the minimum size of an elastic REV (Al-Chalabi, 2014). Furthermore, as defined by Sheriff (2002),
545 the detectable limit in seismic is “the minimum thickness for a bed to give a reflection that stands out above
546 the background”. It has a size equal to a thirtieth of the wavelength size (Sheriff and Geldart, 1995).

547

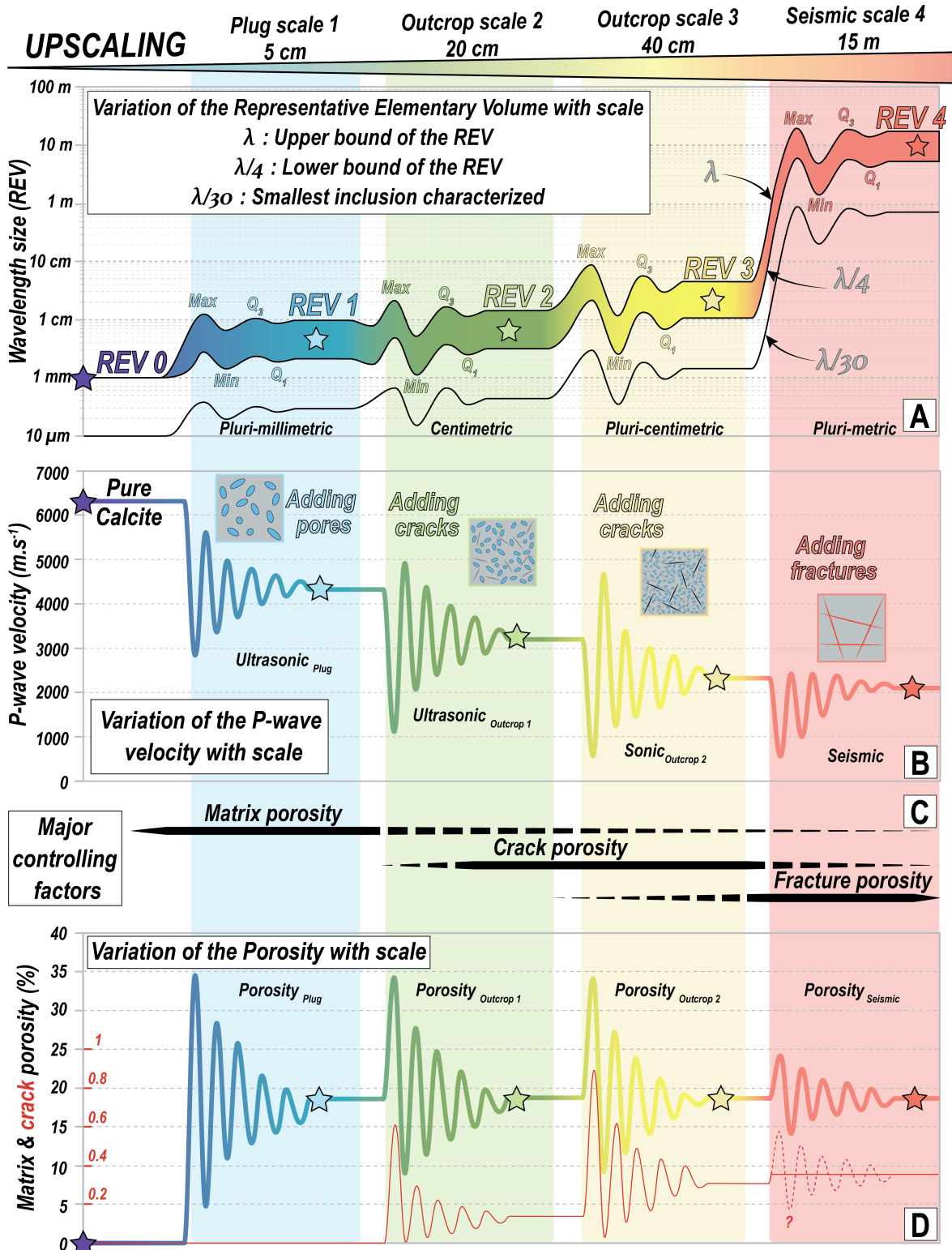
548 Between ultrasonic (~MHz) and seismic (~Hz) measurements, the change of frequency implies a
549 variation of wavelength size, from millimetric to metric (Figure 15a). This upscaling implies a change of
550 the characterized geological object. At plug scale (~ 5 cm of investigation, blue zone of Figure 15), the P-
551 wave velocity is lower than the velocity of calcite and fluctuates because of the intrinsic variability of matrix
552 porosity composed of micro/millimetric pores (Figure 15b). It has to be noted that the fluctuations observed
553 in this dataset are related to the variation of the total porosity and the pore shapes, as already suggested by
554 several authors (Anselmetti and Eberli, 1993; Eberli et al., 2003; Fortin et al., 2007; Soete et al., 2015;
555 Fournier et al., 2018; Regnet et al., 2019a, b). Then, the upscaling to the outcrop scale 2 (~ 20 cm of
556 investigation for the green zone of Figure 15) is again associated with a decrease of the P-wave velocity.
557 Indeed, for that scale, the fluctuations of the P-wave velocity (Figure 15b) are controlled by both the crack
558 and matrix porosity (Figures 14b and 15c, d). Going a step further with measurements at the outcrop scale 3
559 (~ 40 cm of investigation for the yellow zone of Figure 15) aims to highlight this conclusion. The P-wave
560 velocity decreases because of an increasing crack-related porosity. These “scale effects” were already
561 pointed out by Matonti et al. (2015) who also attribute the upscaled P-wave velocity decrease to the
562 occurrence of outcropping structural features. Finally, at the seismic scale 4, the pluri-metric REV 4
563 highlights P-wave velocities is slightly lower than outcrop scale 3, implying that another scale of crack
564 porosity materialized by metric fractures and bedding planes. Despite this slight difference, the mean P-
565 wave velocity of the outcrop scale 3 is very close to the one acquired at seismic scale (Figure 15b),
566 suggesting that a medium of 40 cm in length is representative of the seismic scale. This finding is of
567 importance for upscaling procedures because it shows that sonic measurements (here of 54 kHz) may better

568 correspond to seismic velocities (here of 100 Hz), while ultrasonic measurements on plugs and outcrops
569 (respectively of 500 kHz and 250 kHz) do not fit with seismic acquisition.

570

571 This brings the usual question of the representativeness of plug measurements for reservoir
572 characterization (Ringrose et al., 2008; Corbett et al., 2015). Indeed, by analogy, several authors show that
573 multi-scale geological medium implies different fluid-flow properties that has to be related to multiscale
574 REVs (Nordahl & Ringrose, 2008; Ringrose et al., 2008; Corbett, 2009; Claes, 2015; Ringrose and
575 Bentley, 2015). Similarly here, the upscaling of elastic properties of lacustrine carbonates shows that we
576 need to take into account several scales of rock heterogeneities, from microscopic to megascopic scales,
577 including pores, cracks and fractures, following thus the early works of Stierman and Kovach (1979) as
578 well as Moos and Zoback (1983). The present work highlights the need to interpret and model multiscale
579 elastic data with regards to the different length scales related to geology (Figures 1 and 12). This is of
580 importance for linking high frequency and low frequency elastic moduli because an elastic wave with
581 different frequencies will not necessarily characterize the same geological object. This fact goes against the
582 assumption often made that the drained moduli (equal to the dry elastic moduli) is the same whatever the
583 frequency. Indeed, the geological medium is not homogeneous with scale, implying that it does not
584 necessarily have the same multi-scale elastic properties (Figure 15).

585



586
 587
 588
 589
 590
 591

Figure 15. Upscaling of (a) the wavelength size (REV), (b) P-wave velocity, (c) major controlling factors and (d) porosity versus arbitrary scale of measurements. The curve starts from the pure calcite value and fluctuates with scale changes. For the REV, the descriptive statistics introduced in Figure 9 are used to symbolize the variability. Then, for P-wave velocity and porosity, each fluctuation of the curve represents 10 % of the dataset (deciles), until arriving on the median value symbolized by a plateau.

592 **Conclusion**

593

594 This multi-scale geophysical characterization enables the linkage of elastic properties of
595 dry lacustrine carbonates to relative proportions of crack/fracture porosity. If upscaling of the elastic
596 properties is largely discussed in the literature, there is a paucity of multi scale acoustic field datasets.
597 Indeed, the originality of this work is to compare different scales of acoustic measurements, from ultrasonic
598 to seismic frequency, acquired on the same geological object, keeping in mind the size of the elastic REV
599 - the wavelength size - induced by the used geophysical tools. The large dataset acquired at all scales allow
600 us to have an approach which is statistically effective. Results show that P-wave velocities decrease with
601 decreasing frequency, so that the acoustic measurements are related to the REV evolution and thus to the
602 size of geological features. Indeed, upscaling of elastic properties from ultrasonic (microscopic scale) to
603 seismic (megascopic scale) frequencies means increasing the REV, from pluri-millimetric to pluri-metric.
604 Furthermore, results also show that acoustic measurements done at a frequency of 54 kHz (scale of ~ 40 cm)
605 are really close to the one acquired at 100 Hz, suggesting that sonic velocities can be extrapolated to the
606 seismic frequencies at least for the study site that we investigated. Using effective medium theory, a model
607 based on the comparison of the multiscale datasets is presented (concept of multi-scale REVs). It aims to
608 upscale P-wave velocity assuming that inclusions with different aspect ratios ($\alpha_{matrix\ pores} = 0.15$ and α_{crack-
609 $fractures} = 10^{-3}$) control the elastic behavior of the studied lacustrine carbonates. In our study, model-based
610 results suggest that the crack density/porosity becomes the main controlling factor of P-wave velocity at
611 seismic scale. Finally, the inherited different scales of geological heterogeneities (pores, cracks, fractures)
612 impact differently the elastic properties. This implies that the common matrix porosity control on ultrasonic
613 wave velocities may be lost with upscaling because of the presence of larger structural features (cracks,
614 fractures and bedding planes), a result that is of importance for the understanding of subsurface reservoir
615 properties (*i.e.* porosity and permeability) using solely sonic and seismic data.

616 **Acknowledgments, Samples, and Data**

617 This work is supported by IFP Energies Nouvelles (grant XFP32/001). It is a part of the PhD project of the
 618 first author, at IFP Energies Nouvelles and Laboratoire de Géologie of Ecole normale supérieure. We thank
 619 Ariel Gallagher for the reviewing of the English of this manuscript. We also thank Jo Garland, an
 620 anonymous reviewer and Editor Yves Bernabé for their constructive comments which helped to
 621 significantly improve the manuscript.

622

<i>Thickness (m)</i>	<i>Laboratory dataset</i>					<i>Outcrop dataset</i>		
	<i>Sample name</i>	<i>Density dry</i>	<i>Porosity</i>	<i>Vp dry 500 kHz</i>	<i>Vs dry 500 Khz</i>	<i>Vp 250kHz Horizontal</i>	<i>Vp 54kHz Horizontal</i>	<i>Vp 54kHz Vertical</i>
0.2	RE001	2.15	0.206	4192	2264	1986	1267	2090
0.4	RE002	2.34	0.137	4744	2889	3945	1793	1779
0.6	RE003	2.017	0.256	3504	2259	2160	1406	1306
0.8	RE004	2.34	0.136	4523	2752	2766	3033	1149
1	RE005	2.288	0.155	4566	2575	3161	1870	1263
1.2	RE006	2.164	0.201	4166	2451	2919	3030	1457
1.4	RE007	2.124	0.216	3802	2200	3546	3443	1449
1.6	RE008	2.283	0.157	4802	2803	3175	3478	2550
1.8	RE009	2.322	0.143	4385	2554	3328	3443	1698
2	RE010	2.329	0.141	4545	2775	2964	2278	2401
2.2	RE011	2.284	0.156	4550	2717	2660	2338	2166
2.4	RE012	2.334	0.137	4564	2743	2941	2365	2533
2.8	RE014	2.358	0.129	4959	2864	4348	1309	998
3						3140	2366	2067
3.2	RE015	2.194	0.19	4139	2502	2151	1489	2053
3.4	RE016	2.092	0.228	3789	2264	3373	3429	2768
3.6						3333	2412	3419
3.8	RE018	2.391	0.118	4892	2767	3333	2703	2180
4	RE019	2.201	0.188	4232	2437	3195	2881	2727
4.2	RE020	2.208	0.186	4315	2477	3774	2331	1753
4.4	RE021	2.14	0.211	4019	2333	4141	2576	2117
4.6	RE022	2.252	0.17	4234	2226	2597	2959	3014
4.8	RE023	2.223	0.181	4369	2500	3636	2064	2566
5	RE024	2.349	0.136	4709	2690	3215	1860	1278
5.2	RE025	2.476	0.083	5164	2992	2558	2902	890
5.4	RE026	1.94	0.285	3623	2229	3610	2549	1934
5.6	RE027	1.938	0.285	4025	2270	2090	1461	1875

5.8	RE028	1.917	0.294	3749	2141	2695	3030	1775
6						3759	2901	1412
6.2	RE029	2.34	0.137	4980	2759	3690	2466	2003
6.4	RE032	1.86	0.313	3965	2292	3610	3036	2634
6.6	RE030	2,00	0.262	4172	2373	2594	2096	2340
6.8	RE031	1.988	0.267	4333	2527	1222	1308	
8.2	RE037	1.922	0.284	3249	1996	2717	2812	1630
8.4	RE038	1.844	0.318	3470	2049	2152	1498	2703
8.6	RE039	1.808	0.331	3482	2068	2664	2296	2904
8.8	RE040	2.195	0.191	4166	2519	2845		
9	RE041	2.225	0.176	4528	2724	2284	2998	
9.2	RE042	2.174	0.2	4193	2410	1751	1518	
9.4	RE043	1.911	0.292	3545	2128	2532	1724	2703
9.6	RE044	1.957	0.278	3615	2142	2320	1208	
9.8	RE045	1.951	0.278	3712	2181	2421	1331	
10	RE046	2.296	0.154	4552	2509	1591		
10.2	RE047B	1.817	0.329	3137	1891	2500	597	
10.4	RE048	1.77	0.346	3082	1888	2963	2817	
10.6	RE049	1.784	0.342	3362	1996	3846		
10.8	RE050	2.181	0.197	4101	2419	2733		
11						3409		
11.4	RE053	2.358	0.133	3830	2291	0		
11.8	RE054	2.467	0.093	4228	2581	4375		
12	RE055	2.416	0.111	4690	2802	4400		
12.2	RE056	2.533	0.068	5016	2945	0		
12.6	RE057	2.128	0.215	4235	2387	0		
12.8	RE058	2.29	0.153	4719	2719	0		
13.2	RE059	2.175	0.199	3983	2364	3750		
13.4	RE060	2.207	0.187	4323	2677	2848		
13.6	RE061	2.323	0.144	4871	2870	1452		
13.8	RE062	2.122	0.218	4020	2572	4531		
14	RE063T	2.018	0.254	3910	2263	4437		
14.2						3614	1031	
14.4	RE064	2.31	0.149	4473	2621	2759	1391	2794
14.6	RE065	2.371	0.127	4766	2790	4389		
23.4						4107	3374	3340
23.6	RE106	2.25	0.167	4608	2626	3987	3468	2118
23.8	RE107	2.31	0.143	4713	2687	3830	2238	2661
24	RE108	2.485	0.073	5601	3077	4319	2946	2517
24.2	RE109	2.221	0.182	4711	2483	2381	1121	1499
24.4	RE110	1.998	0.263	3821	2213	2419	912	1426
24.6	RE111	2.304	0.148	4958	2674	2512	995	989
24.8	RE112	2.371	0.123	4693	2800			
25						2365	2196	
26.6	RE066	2.408	0.114	4613	2770	4854	2785	

26.8						3431	1814	1518
27	RE067	2.185	0.194	4298	2489	3096	1662	1021
27.2	RE068	2.424	0.104	4948	2808	3745	2037	990
27.4	RE069	2.317	0.144	4465	2651	4415	3219	2721
27.6	RE070	2.376	0.123	4990	2613	4914	3904	
28.6	RE071	2.453	0.08	5403	2796	4415	2765	
28.8	RE072	2.409	0.112	4713	2643	4515	3330	
29	RE073	2.412	0.11	4933	2643	3974	4204	2006
32						2432	1496	
32.2	RE074	2.092	0.229	4070	2515	3257	1627	1081
32.4	RE075	2.154	0.205	4346	2538	3257	2440	3053
32.6	RE076	2.195	0.191	4430	2607	4073	2946	
32.8	RE077	2.32	0.141	4881	2708		3337	
33	RE078	2.175	0.199	4391	2299	3731	2682	2466
33.2	RE079	2.096	0.226	4010	2379	3552	562	
33.4	RE080	1.931	0.288	3523	2066	3552	1297	3234
33.6	RE081	2.323	0.144	4782	2639		2577	944
33.8	RE082	2.438	0.097	4990	2653	3906	1692	1372
34.2	RE083	2.46	0.094	5197	2809	2571		
34.4	RE084	2.336	0.14	4488	2717	4762	1645	
34.6	RE085	2.399	0.116	5164	2931	4787	1255	
34.8	RE086	2.316	0.146	4865	2663	4219	1859	
35	RE087	2.01	0.259	3588	2072	2109	1498	
35.2	RE088	2.572	0.054	4837	2727	3221		
35.4						1127		
35.6	RE089	2.396	0.117	5322	2850	1270		
35.8	RE090	2.276	0.162	4632	2521			
36	RE091	2.583	0.048	4565	2867	3712		
36.2						2913		
37.2	RE093	2.064	0.24	3124	1792			
37.4	RE094	2.088	0.23	3091	1888			
37.6	RE095	2.007	0.26	2877	1784			
38	RE096	2.094	0.231	3773	2026	1462		
38.2						3425	4663	
38.4							2872	2491
38.6	RE098	2.202	0.189	3993	2444	3236		
38.8	RE099	2.318	0.146	4127	2390	1950	1064	
39						2941		
39.2	RE101	2.15	0.208	3135	1986	2005		
40	RE102	2.029	0.253	3070	1736	2120		
40.2	RE103	2.036	0.251	3167	1886	3604	2283	2003
40.4	RE104	1.848	0.319	2859	1755			
40.6	RE105	2.195	0.192	4025	2272			

624 **References**

- 625 Adam, L., Batzle, M., & Brevik, I. (2006). Gassmann's fluid substitution and shear modulus variability in
626 carbonates at laboratory seismic and ultrasonic frequencies. *GEOPHYSICS*, *71*(6), F173–F183.
627 <https://doi.org/10.1190/1.2358494>
- 628 Adelinet, M., Fortin, J., & Guéguen, Y. (2011). Dispersion of elastic moduli in a porous-cracked rock:
629 Theoretical predictions for squirt-flow. *Tectonophysics*, *503*(1–2), 173–181.
630 <https://doi.org/10.1016/j.tecto.2010.10.012>
- 631 Adelinet, M., Domínguez, C., Fortin, J., & Violette, S. (2018). Seismic-refraction field experiments on
632 Galapagos Islands: A quantitative tool for hydrogeology. *Journal of Applied Geophysics*, *148*, 139–
633 151. <https://doi.org/10.1016/j.jappgeo.2017.10.009>
- 634 Al-Chalabi, M., 2014. Principles of Seismic Velocities and Time-to-Depth Conversion, *EAGE*
635 *Publications*, 491 p.
- 636 Anselmetti, F. S., & Eberli, G. P. (1993). Controls on sonic velocity in carbonates. *Pure and Applied*
637 *Geophysics PAGEOPH*, *141*(2–4), 287–323. <https://doi.org/10.1007/BF00998333>
- 638 Baechle, G. T., Weger, R. J., Eberli, G. P., Massafiero, J. L., & Sun, Y.-F. (2005). Changes of shear moduli
639 in carbonate rocks: Implications for Gassmann applicability. *The Leading Edge*, *24*(5), 507–510.
640 <https://doi.org/10.1190/1.1926808>
- 641 Baechle, G. T., Colpaert, A., Eberli, G. P., & Weger, R. J. (2008). Effect of microporosity on sonic velocity
642 in carbonate rocks. *The Leading Edge*, *17*, <https://doi.org/10.3997/2214-4609.201404934>
- 643 Bailly, C., Adelinet, M., Hamon, Y., & Fortin, J. (2019). Combined control of sedimentology and diagenesis
644 on seismic properties in lacustrine and palustrine carbonates (Upper Miocene, Samos Island, Greece).
645 *Geophysical Journal International*, 2019, *212*(2), 1300–1315.

- 646 Bear, J. (1972). *Dynamics of Fluids in Porous Media*, 784 pp., American Elsevier Publishing Compagny,
647 New York.
- 648 Benveniste, Y. (1987). A new approach to the application of Mori-Tanaka's theory in composite materials.
649 *Mechanics of Materials*, 6(2), 147–157. [https://doi.org/10.1016/0167-6636\(87\)90005-6](https://doi.org/10.1016/0167-6636(87)90005-6)
- 650 Borgomano, J. V. M., Pimienta, L., Fortin, J., & Guéguen, Y. (2017). Dispersion and attenuation
651 measurements of the elastic moduli of a dual-porosity limestone. *Journal of Geophysical Research:*
652 *Solid Earth*, 122(4), 2690–2711. <https://doi.org/10.1002/2016JB013816>
- 653 Bourbié, T., Coussy, O., & Zinszner, B. (1987). *Acoustics of porous media*, Editions Technip, Gulf
654 Publishing Company, Houston, TX (TECHNIP)
- 655 Cichostępski, K., Dec, J., & Kwietniak, I. (2019) Simultaneous Inversion of Shallow Seismic Data for
656 Imaging of Sulfurized Carbonates. *Minerals*, 9(4), 203. <https://doi.org/10.3390/min9040203>
- 657 Claes, S. (2015). *Pore classification and upscaling strategy in travertine reservoir rocks*, 119 pp., PhD
658 Thesis, Katholieke Universiteit Leuven.
- 659 Corbett, P. W. M. (2009). *Petroleum Geoengineering : Integration of Static and Dynamic Models*, 100 pp.,
660 Society of Exploration Geophysicists, Tulsa, Oklahoma.
- 661 Corbett, P. W. M., Hayashi, F. Y., Alves, M. S., Jiang, Z., Wang, H., Demyanov, V., et al. (2015). Microbial
662 carbonates: a sampling and measurement challenge for petrophysics addressed by capturing the
663 bioarchitectural components. *Geological Society, London, Special Publications*, 418(1), 69–85.
664 <https://doi.org/10.1144/sp418.9>
- 665 David, E. C., & Zimmerman, R. W. (2011a). Compressibility and shear compliance of spheroidal pores:
666 Exact derivation via the Eshelby tensor, and asymptotic expressions in limiting cases. *International*
667 *Journal of Solids and Structures*, 48(5), 680–686. <https://doi.org/10.1016/j.ijsolstr.2010.11.001>

668 David, E. C., & Zimmerman, R. W. (2011b). Elastic moduli of solids containing spheroidal pores.
669 *International Journal of Engineering Science*, 49(7), 544–560.
670 <https://doi.org/10.1016/j.ijengsci.2011.02.001>

671 Eberli, G. P., Baechle, G. T., Anselmetti, F. S., & Incze, M. L. (2003). Factors controlling elastic properties
672 in carbonate sediments and rocks. *The Leading Edge*, 22(7), 654–660.
673 <https://doi.org/10.1190/1.1599691>

674 Fortin, J., Guéguen, Y., & Schubnel, A. (2007). Effects of pore collapse and grain crushing on ultrasonic
675 velocities and V_p/V_s . *Journal of Geophysical Research: Solid Earth*, 112(8).
676 <https://doi.org/10.1029/2005JB004005>

677 Fournier, F., Leonide, P., Biscarrat, K., Gallois, A., Borgomano, J., & Foubert, A. (2011). Elastic properties
678 of microporous cemented grainstones. *GEOPHYSICS*, 76(6), E211–E226.
679 <https://doi.org/10.1190/geo2011-0047.1>

680 Fournier, F., Léonide, P., Kleipool, L., Toullec, R., Reijmer, J. J. G., Borgomano, J., et al. (2014). Pore
681 space evolution and elastic properties of platform carbonates (Urgonian limestone, Barremian-
682 Aptian, SE France). *Sedimentary Geology*, 308, 1–17. <https://doi.org/10.1016/j.sedgeo.2014.04.008>

683 Fournier, F., Pellerin, M., Villeneuve, Q., Teillet, T., Hong, F., Poli, E., et al. (2018). The equivalent pore
684 aspect ratio as a tool for pore type prediction in carbonate reservoirs. *AAPG Bulletin*, 102(7), 1343–
685 1377. <https://doi.org/10.1306/10181717058>

686 Haldorsen, H. H., & Lake, L. W. (1984). A New Approach to Shale Management in Field-Scale Models.
687 *Society of Petroleum Engineers Journal*, 24(04), 447–457. <https://doi.org/10.2118/10976-pa>

688 Jeanne, P., Guglielmi, Y., & Cappa, F. (2012). Multiscale seismic signature of a small fault zone in a
689 carbonate reservoir: Relationships between V P imaging, fault zone architecture and cohesion.
690 *Tectonophysics*, 554–557, 185–201. <https://doi.org/10.1016/j.tecto.2012.05.012>

691 Marion, D., & Jizba, D. (1997). Acoustic properties of carbonate rocks: Use in quantitative interpretation
692 of sonic and seismic measurements, *In : Palaz, I, and Marfurt, K.J., eds., Carbonate Seismology:*
693 *Geophysical Developments*. Society of Exploration Geophysicists, Tulsa, Oklahoma, 75–93.

694 Matonti, C., Guglielmi, Y., Viseur, S., Bruna, P. O., Borgomano, J., Dahl, C., & Marié, L. (2015).
695 Heterogeneities and diagenetic control on the spatial distribution of carbonate rocks acoustic
696 properties at the outcrop scale. *Tectonophysics*, 638(1), 94–111.
697 <https://doi.org/10.1016/j.tecto.2014.10.020>

698 Mavko, G., Mukerji, T. ; & Dvorkin, J. (2009) *The Rock Physics Handbook: Tools for Seismic Analysis of*
699 *Porous Media*, 524 pp., Cambridge Univ. Press, Cambridge, U.K.

700 Moos, D., & Zoback, M. D. (1983). In Situ Studies of Velocity in Fractured Belair Belt. *J. Geophys. Res.*,
701 88(2), 2345–2358.

702 Nordahl, K. (2004). *A petrophysical evaluation of tidal heterolithic deposits: Application of a near wellbore*
703 *model for reconciliation of scale dependant well data*, 338 pp., PhD Thesis, Norwegian University
704 of Science and Technology.

705 Nordahl, K., & Ringrose, P. S. (2008). Identifying the representative elementary volume for permeability
706 in heterolithic deposits using numerical rock models. *Mathematical Geosciences*, 40(7), 753–771.
707 <https://doi.org/10.1007/s11004-008-9182-4>

708 Owen, R. B., Renaut, R. W., & Stamatakis, M. G. (2011). Late Miocene lacustrine sedimentation in the
709 Mytilinii Basin, Samos Island, Greece. *Journal of Paleolimnology*, 46(1), 151–166.
710 <https://doi.org/10.1007/s10933-011-9530-0>

711 Panza, E., Agosta, F., Rustichelli, A., Vinciguerra, S. C., Ougier-Simonin, A., Dobbs, M., & Prosser, G.
712 (2019). Meso-to-microscale fracture porosity in tight limestones, results of an integrated field and

713 laboratory study. *Marine and Petroleum Geology*, 103, 581–595.
714 <https://doi.org/10.1016/j.marpetgeo.2019.01.043>

715 Raymer, L. L., Hunt, E. R., & Gardner, J. S. (1980). An Improved Sonic Transit Time-to-Porosity
716 Transform. In *SPWLA Annual Logging Symposium*, 1–13. Society of Petrophysicists and Well-Log
717 Analysts.

718 Regnet, J. B., Robion, P., David, C., Fortin, J., Brigaud, B., & Yven, B. (2015). Acoustic and reservoir
719 properties of microporous carbonate rocks: Implication of micrite particle size and morphology.
720 *Journal of Geophysical Research: Solid Earth*, 120(2), 790–811.
721 <https://doi.org/10.1002/2014JB011313>

722 Regnet, J., Fortin, J., Nicolas, A., Pellerin, M., & Guéguen, Y. (2019a). Elastic properties of continental
723 carbonates: From controlling factors to an applicable model for acoustic-velocity predictions.
724 *GEOPHYSICS*, 84(1), MR45–MR59. <https://doi.org/10.1190/geo2017-0344.1>

725 Regnet, J. B., David, C., Robion, P., & Menéndez, B. (2019b). Microstructures and physical properties in
726 carbonate rocks: A comprehensive review. *Marine and Petroleum Geology*. Elsevier.
727 <https://doi.org/10.1016/j.marpetgeo.2019.02.022>

728 Ring, U., Laws, S., & Bernet, M. (1999). Structural analysis of a complex nappe sequence and late-orogenic
729 basins from the Aegean Island of Samos, Greece. *Journal of Structural Geology*, 21(11), 1575–1601.
730 [https://doi.org/10.1016/S0191-8141\(99\)00108-X](https://doi.org/10.1016/S0191-8141(99)00108-X)

731 Ringrose, P. S., Martinius, A. W., & Alvestad, J. (2008). Multiscale geological reservoir modelling in
732 practice. *Geological Society, London, Special Publications*, 309(1), 123–134.
733 <https://doi.org/10.1144/SP309.9>

734 Ringrose, P., & Bentley, M. (2015). *Reservoir Model Design: A Practitioner's Guide*. 249 pp., Springer
735 Netherlands. [https://doi.org/DOI 10.1007/978-94-007-5497-3](https://doi.org/DOI%2010.1007/978-94-007-5497-3)

- 736 Sheriff, R.E., Geldart, L. P. (1995). *Exploration seismology*, 592 pp., Cambridge University Press.
- 737 Sheriff, R. E. (2002). *Encyclopedic Dictionary of Exploration Geophysics*, 442 pp., Society of Exploration
738 Geophysicists.
- 739 Soete, J., Kleipool, L. M., Claes, H., Claes, S., Hamaekers, H., Kele, S., et al. (2015). Acoustic properties
740 in travertines and their relation to porosity and pore types. *Marine and Petroleum Geology*, 59, 320–
741 335. <https://doi.org/10.1016/j.marpetgeo.2014.09.004>
- 742 Stamatakis, M. G., Hein, J. R., & Magganas, A. C. (1989). Geochemistry and diagenesis of Miocene
743 lacustrine siliceous sedimentary and pyroclastic rocks, Mytilinii Basin, Samos Island, Greece.
744 *Sedimentary Geology*, 64, 65–78. [https://doi.org/https://doi.org/10.1016/0037-0738\(89\)90084-5](https://doi.org/10.1016/0037-0738(89)90084-5)
- 745 Stierman, D. J., & Kovach, R. L. (1979). An in situ velocity study: The Stone Canyon Well. *Journal of*
746 *Geophysical Research: Solid Earth Solid Earth*, 84(B2), 672–678.
747 <https://doi.org/10.1029/JB084iB02p00672>
- 748 Verwer, K., Braaksma, H., & Kenter, J. A. (2008). Acoustic properties of carbonates: Effects of rock texture
749 and implications for fluid substitution. *GEOPHYSICS*, 73(2), B51–B65.
750 <https://doi.org/10.1190/1.2831935>
- 751 Walsh, J. B. (1965). The effect of cracks on the compressibility of rock. *Journal of Geophysical Research*,
752 70(2), 381–389. <https://doi.org/10.1029/jz070i002p00381>
- 753 Wang, Z., Hirsche, W. K., & Sedgwick, G. (1991). Seismic velocities in carbonate rocks. *Journal of*
754 *Canadian Petroleum Technology*, 30(2), A354. [https://doi.org/https://doi.org/10.2118/91-02-09](https://doi.org/10.2118/91-02-09)
- 755 Weidmann, M., Solounias, N., Drake, R. E., & Curtis, G. H. (1984). Neogene Stratigraphy of the Eastern
756 Basin,. *Geobios*, 17(4), 477–490.

- 757 Wollner, U., & Dvorkin, J. (2018). Seismic-scale dependence of the effective bulk modulus of pore fluid
758 upon water saturation. *GEOPHYSICS*, 83(2), MR81–MR91. <https://doi.org/10.1190/geo2017->
759 0293.1
- 760 Wyllie, M. R., Gregory, A. R., & Gardner, G. H. F.. (1956). Elastic wave velocities in heterogeneous and
761 porous media, *GEOPHYSICS*, 21, 41–70. doi:10.1190/1.1438217
- 762 Xu, S., & Payne, M. A. (2009). Modeling elastic properties in carbonate rocks. *The Leading Edge*, 28(1),
763 66–74.